

1
2
3
4
5
6
7
8
9
10
11
12
13
14
15
16
17
18
19
20
21
22
23
24
25
26
27

A geological explanation for intraplate earthquake clustering complexity: the zeolite-bearing fault/fracture networks in the Adamello Massif (Southern Italian Alps)

E.D. Dempsey¹, R.E. Holdsworth¹, J. Imber¹, A. Bistacchi² and G. Di Toro^{3,4}

1 = Dept of Earth Sciences, Durham University, Durham, UK

2 = Dipartimento di Scienze Geologiche e Geotecnologie, Università degli Studi di Milano Bicocca, Milano, Italy

3 = Dipartimento di Geoscienze, Università degli Studi di Padova, Padova, Italy

4 = Istituto Nazionale di Geofisica e Vulcanologia, Roma, Italy.

Corresponding Author:

E.D. DEMPSEY

Dept of Earth Sciences,

Science Block,

Durham University,

Durham,

DH1 3LE,

UK

Telephone: +44 (0) 191 3342356

Email: e.d.dempsey@durham.ac.uk

28

29 **Abstract:** Interconnected networks of faults and veins filled with hydrothermal minerals such
30 as zeolite are widespread in many orogenic terrains. These fractures commonly form at
31 relatively low temperatures (e.g. $< 200^{\circ}\text{C}$) late in the tectonic history and represent
32 significant phases of fluid flow and mineralisation during exhumation. Zeolite-bearing
33 fractures spatially associated with the Gole Larghe Fault Zone in the Southern Italian Alps
34 are preserved along an interconnected network of variably orientated pre-existing structures.
35 They show evidence of repeated episodes of hydraulic tensile fracturing and small magnitude
36 (total offsets $< 5\text{m}$) shear displacements. We use geological observations and Coulomb stress
37 modelling to propose that repeated seismogenic rupturing of larger offset faults led to local
38 stress transfer and reactivation of widely distributed smaller pre-existing structures in the wall
39 rocks. The differing orientations of the pre-existing features within what is assumed to have
40 been a single regional stress field led to the simultaneous development of reverse, strike-slip
41 and extensional faults. The kinematic diversity and cyclic nature of the hydraulically-assisted
42 deformation suggest that the mineralised fracture systems represent a geological
43 manifestation of intraplate micro-earthquake clusters associated with fluid migration episodes
44 in the upper crust. Our observations highlight the role of crustal fluids and structural
45 reactivation during earthquakes.

46

47

48

49

50

51 **1. Introduction**

52 It is well-known that some lower magnitude earthquake clusters are spatially and
53 temporally associated with larger mainshock events along faults: these are referred to as *fore-*
54 *and after-shock sequences* (e.g. Scholz, 2002 and references therein). In other instances
55 multiple lower magnitude seismic events may be closely spaced in time and space, but no
56 main shock is observed: these are known as *swarms* (Sykes 1970; Mogi, 1963). The latter are
57 often – but by no means always – associated with volcanic or geothermal activity, whilst
58 some may be artificially induced by fluid injection (e.g. see Fischer *et al.* 2013 and references
59 therein).

60 The origins of the frequently observed kinematic and spatial complexity associated
61 with low magnitude earthquakes – as illustrated, respectively, by their complex focal
62 mechanism solutions and diffuse, cloud-like distributions (e.g. Shearer *et al.* 2003, Godano *et*
63 *al.* 2013, Kassaras *et al.* 2014) – are matters of speculation and debate. In general, clustering
64 activity seems to be strongly associated with fluid ingress: the stress perturbation induced
65 by each event results in stress and fluid redistribution and, as a consequence, in the complex
66 spatial evolution of the sequence (Kisslinger, 1975; Main, 1996). A number of authors have
67 already tried use geological observations to make inferences about past seismogenic
68 clustering behaviour along fault and fracture systems exposed at the surface (e.g. Sibson
69 1985a; Micklethwaite & Cox 2004, 2006; Kirkpatrick *et al.* 2008). Others have used
70 theoretical approaches such as the use of slip tendency analyses to address this issue (e.g.
71 Collettini & Trippetta 2007). Key questions for structural geologists studying ancient brittle
72 structures are: what might such foreshock-aftershock/earthquake sequences or swarms look
73 like in rocks, why are they diffuse in their distribution and why might they sometimes be
74 kinematically complex?

75 In this paper, we discuss this problem from a geological perspective, documenting
76 well-exposed examples of zeolite-mineralised fractures associated with a linked, distributed
77 system of reverse, strike-slip and extensional faults developed close to the well-known Gole
78 Larghe Fault Zone cutting the Adamello Massif in the Italian Alps. The spatial and geometric
79 diversity of these fractures is shown to result from the hydraulically-assisted reactivation of
80 pre-existing structures occupying at least 0.5 cubic kilometres of the granitic host rocks. We
81 investigate whether, on the reasonable assumption that the fracture sets formed
82 seismogenically, the observed geometric and kinematic relationships represent the geological
83 manifestation of foreshock-aftershock sequences and/or earthquake swarms in an intraplate
84 setting.

85

86 **2. Regional setting**

87 The Adamello Massif lies in the South Alpine Domain of the Italian Alps and is a
88 tonalitic batholith located near to the intersection of the Giudicarie and Tonale segments of
89 the Periadriatic fault system (Fig. 1a; Bianchi & Dal Piaz, 1937; Bianchi *et al.*, 1970).
90 According to Callegari (1985) and Callegari & Brack (2002), there are four distinct tonalitic–
91 granodioritic intrusions: 1) Re di Castello–Corno Alto; 2) Adamello; 3) Val d’Avio-Val di
92 Genova; 4) Presanella. Geochronological data (Del Moro *et al.*, 1983, Hansmann & Oberli,
93 1991, Viola *et al.*, 2001, Mayer *et al.*, 2003 and Stipp *et al.*, 2004) indicate a progressive
94 decrease in the age of these intrusive units from S to N (Re di Castello: 42–38 Ma;
95 Presanella: 32–30 Ma; Pennacchioni *et al.*, 2006). Mineral assemblages preserved in the
96 aureole of the batholith suggest syn-emplacement pressures in the region of 0.25–0.35 GPa,
97 which corresponds to depths in the region of 9–11 km assuming typical rock densities (Stipp *et*
98 *al.* 2004).

99 The country rocks along the northern border of the Adamello massif were sheared
100 during dextral strike-slip movement of the Tonale Fault (30-32 Ma; Stipp *et al.* 2004;
101 Pennacchioni *et al.* 2006). Post-magmatic, solid-state deformation structures are widely
102 documented in the Val d'Avio-Val di Genova and Presanella plutons and record a
103 progressive down-temperature history of deformation during exhumation of the pluton (Di
104 Toro & Pennacchioni, 2004; Pennacchioni *et al.*, 2006; Mittempergher *et al.*, 2009). These
105 structures include: cooling joints and aplite dykes formed at elevated temperatures (>600°C);
106 conjugate dextral and sinistral ductile shear zones (550-450°C); mainly dextral epidote-
107 chlorite-bearing cataclasites and pseudotachylytes (300-250°C); and late stage zeolite-bearing
108 faults and veins (<200°C) (Pennacchioni *et al.*, 2006). Larger-scale dextral faults and shear
109 zones associated with the development of the main brittle deformation stage (epidote-
110 chlorite-bearing cataclasites and pseudotachylytes) include the NW-SE Passo Cercen Fault
111 Zone in the north together with the E-W to ESE-WNW-trending Gole Larghe Fault Zone
112 (GLFZ) and Lares Fault Zone in the south (Fig 1a). On a regional scale, these structures are
113 viewed as offshoots of the Tonale Fault. The Tonale Fault is also thought by some authors to
114 be cross cut and offset by up to 20km in a sinistral sense by the younger (< 17Ma) Giudicarie
115 Line, the southern part of which forms the eastern boundary of the Adamello plutons (Fig. 1;
116 see Viola *et al.*, 2001).

117 The rocks of the Adamello pluton are well exposed in the scoured rock platform where
118 the GLFZ crosses the valley at the toe of the Lobbia Glacier (Figs 1b-c). The host rocks of
119 the Val d'Avio-Val di Genova pluton are typically fine-to medium grained tonalites with a
120 bulk mineralogy: 45-50% plagioclase, 25-30% quartz, 15-20% biotite and 1-5% K-feldspar
121 (Di Toro & Pennacchioni 2004). Many previous studies (e.g. Di Toro & Pennacchioni, 2004,
122 2005; Pennacchioni *et al.*, 2006; Bestmann *et al.*, 2012; Smith *et al.*, 2013; Mittempergher *et*
123 *al.*, 2014) have focussed on post-magmatic deformation structures related to the development

124 of the E-W-trending GLFZ. This structure is made up of a series of E-W trending sub-parallel
125 fault strands, dipping steeply S, which carry abundant cataclasites and pseudotachylytes in a
126 composite fault zone 500-600m thick (Di Toro & Pennacchioni 2005; Smith *et al.*, 2013).
127 Shallowly E-dipping slickenline lineations along the faults and shear sense criteria suggest
128 dextral displacements. ^{39}Ar - ^{40}Ar dating of the pseudotachylytes shows that the majority of
129 these friction melts formed ca. 30Ma at depths of 9-11km based on: i) the associated stable
130 fault rock mineral assemblages (K-feldspar-epidote-chlorite); and ii) the preservation of
131 evidence of low temperature plasticity in quartz (Di Toro & Pennacchioni 2004, 2005). These
132 events are broadly coeval with early dextral motions along the Tonale Line (Pennacchioni *et*
133 *al.*, 2006) and pre-date the main phase of exhumation of the Adamello Massif (<22Ma)
134 determined using thermochronology (e.g. Reverman *et al.* 2012).

135 Despite excellent exposure, the later zeolite-bearing structures in the Lobbia Glacier
136 valley have received little attention. They occur in a variety of orientations and are best
137 exposed in an area covering about 1km² over a vertical elevation of at least 500m (including
138 the steep cliffs on either side of the valley) located in the southern, upper part of the GLFZ
139 and its immediate hangingwall rocks (Fig. 1b, c). They belong to a regional suite of late
140 tectonic fracture-hosted zeolite veins and associated alteration zones found throughout the
141 Alps (e.g. see Weisenberger & Bucher 2010). Their precise age is unknown, but it is
142 generally believed that they formed during or following the final exhumation of the Alpine
143 chain, i.e. they are younger than 20Ma and likely developed between 15 and 9 Ma. The
144 depths at which zeolite mineralization developed are uncertain. There is no evidence to
145 suggest that the thermal gradient in the Adamello Massif at this time was significantly greater
146 than its present day value (35°C km⁻¹). Assuming thermal equilibrium between veins and host
147 rocks, the typical zeolite mineralization temperatures of <200°C imply maximum formation
148 depths of <6 km. Recent apatite fission track and ^{40}Ar - ^{39}Ar dating suggest formation depths

149 of >2.5 km (e.g. Weisenberger et al. 2012). There is no structural evidence for tilting of the
150 Adamello batholith during its exhumation from depth (Brack, 1981).

151

152 **3. Zeolite-bearing structures**

153 *3.1. Field observations*

154 The zeolite mineralization is everywhere associated with linked meshes of
155 anastomosing brittle fractures and veins (Figs 2, 3, 4). Three intimately associated styles of
156 fine to ultrafine grained mineralization are recognized: crystalline vein fills (Figs 2a, b),
157 altered damage zones (Figs 2a, c-e) and mineralized cataclasites and gouges (Figs 2c, d, 3a-
158 d). The zeolites form in a wide variety of bright colours, standing out against the pale greys
159 of the host tonalite, including brick red, milky white, yellow and orange-pale brown (Figs 2,
160 3). Many fault zones and veins preserve evidence of later brittle faulting and cataclasis
161 overprinting and reworking earlier zeolite mineralization (e.g. Figs 5a, b). The broader zones
162 of zeolite-hosted fractures are softer than the host tonalities and are prone to preferential
163 erosion forming breaks of slope (e.g. E-W faults T1, T2, T4; Figs 1b, c, 2f) or gully features
164 that may host melt water streams from the glacier (e.g. faults S1, S3, N1, N2; Figs 1b, 2e).

165 Three main groups of zeolite-bearing faults and fractures are recognised based on
166 differences in orientation (here denoted using strike direction) and shear sense (Figs 1-7): i)
167 NNE-SSW sinistral (Figs 2c, e, 3a, b); ii) NNW-SSE to NNE-SSW normal (Figs 2a, 3c); and
168 iii) E-W sinistral-reverse (Figs 2d, f, 3d). All three fracture sets display local hard linkage
169 (e.g. Figs 2e, f, 3e, f, 4) or are mutually cross-cutting, and contain mineralogically and
170 texturally similar fault rocks (Figs 2-7, Table 1). These observations are consistent with the
171 fracture sets being broadly contemporaneous features. Individual fault and fracture zones are

172 rarely more than a few centimetres wide and total fault offsets are small (where it can be
173 determined, most are < 1m). The sinistral faults are associated with the largest displacements
174 based on the magnitudes of measured offsets of geological markers, such as igneous contacts,
175 layering or pre-existing faults (e.g. fault S1 shows a maximum 5m offset). Many zeolite-
176 bearing structures reactivate pre-existing shear zones (e.g. Fig 2c). The displacement
177 estimates are therefore likely to represent the *cumulative* displacement history and should be
178 viewed as upper bounds to the slip along the zeolite-bearing structures. The sinistral faults
179 also preserve the greatest widths of associated mineralised and altered damage zones (up to
180 2m; e.g. faults S1, S2, S3; Fig. 2c, e, 3b).

181 The NNE-SSW sinistral faults are characterised by the development of laterally
182 continuous tabular volumes, up to 2m wide in map view, that contain fracture meshes
183 associated with zeolite-rich gouge (individually <1cm thick) (Figs 2c, 3a, b), thin zeolite
184 mineral veins (each <1cm wide) (Fig. 3a), shallowly- to moderately-plunging slickenfibres
185 lineations (Fig. 3a) and linked arrays of Riedel (R) and P-shears. The density of zeolite-filled
186 minor faults and fractures decreases moving away from the main faults (Fig. 4).

187 The N-S normal faults are characterised by the presence of fracture meshes up to
188 10cm wide (Fig. 2a), finely banded zeolite veins up to 1cm thick and dip-slip slickenfibres
189 lineations (Fig. 3c). A minority of N-S structures show evidence for tensile fracturing with no
190 apparent shearing and fibrous zeolite infills (e.g. Fig. 2b).

191 The E-W sinistral-reverse faults are more heterogeneous. In many exposures, they are
192 little more than clean breaks containing minor amounts of associated fault rock or mineral fill
193 (e.g. faults T2, T4; Fig. 1b). In contrast, parts of some other E-W faults are characterised by
194 broad regions of brittle fracturing and alteration (damage zones) up to 2m wide, especially in
195 regions close to intersections with NNE-SSW striking sinistral faults, where linked arrays of

196 sinistral-reverse faults locally form duplex-like structures (e.g. faults T1, T3; Figs 2d, f, 3d).
197 In fault T1, the thickness of the damage zone tapers down from 2 meters to 10 cm in just few
198 tens of meters moving away from the intersection with the main NNE-SSW striking sinistral
199 fault S1 (Fig. 4). Shear surfaces locally carry zeolite-dominated gouge and cataclasite (Figs
200 2d, 3d), oblique-slip slickenfibres lineations and R shears (Figs 3d). The footwalls of the
201 larger E-W faults (T1, T3) are locally hard linked to sub-vertical N-S trending tensile fracture
202 systems (up to 2 cm wide) filled with injected orange-brown zeolite gouge and, locally,
203 breccia (e.g. see Fig. 6a-d) that extend several metres down into the immediate footwall
204 rocks.

205 In summary, three kinematically distinct hard-linked and mutually cross-cutting fault
206 sets and fracture meshes are associated with syn-deformational zeolite mineralization in the
207 Lobbia Glacier valley. The NNE-SSW striking sinistral faults mostly re-activate small
208 sinistral mylonitic shear zones. A proportion of the cumulative displacement might have been
209 accommodated during slip along the mylonitic shear zones at $\sim 500^{\circ}\text{C}$. As a consequence, the
210 cumulative slip associated to the zeolite-facies deformation ($< 200^{\circ}\text{C}$) event is difficult to
211 constrain with precision. However, the NNE-SSW striking sinistral faults are interpreted as
212 the master faults because: (1) they are associated with the thickest zones of zeolite
213 mineralization; and (2) the damage zone thicknesses of the E-W striking faults decreases
214 moving away from where they intersect with the NNE-SSW striking faults (Fig. 4).

215 *3.2. Mineralogical and microstructural observations*

216 Regardless of movement sense, all fault rocks, alteration zones and mineral fills are
217 associated with the same zeolite mineralization. This compositional consistency was verified
218 using X-ray diffraction analysis (Table 1, Appendix 1). The main mineral cements found
219 were zeolites (Ca-rich stilbite, scolecite and stellerite, together with the Na- and Ca-rich

220 laumontite) and prehnite. Such a mineral assemblage is typical of precipitation from CO₂-
221 poor, alkaline-rich aqueous fluids at T < 200°C and P < 200MPa (Deer et al., 1992;
222 Weisenberger & Bucher 2010, 2012). Fluid-rock interactions are evident from the observed
223 widespread alteration of host plagioclase feldspars, with many zeolite-hosted veins, fault
224 zones and fractures displaying pale alteration haloes up to several cm thick (e.g. Figs 2a, d,
225 3b, 5b).

226 Many N-S and NNE-SSW structures seem to develop initially as tensile/hybrid
227 fractures hosting composite zoned zeolite veins (e.g. Figs 2b, 3a, 5a, 5b), with anhedral
228 zeolites at the vein walls and fine-grained acicular zeolites towards the centre (Fig. 7a).
229 Crack-seal textures are locally preserved and are consistent with repeated fluid flow events
230 during fracturing (e.g. Cox 1987; Sibson *et al.*, 1988; and Hilgers & Urai 2005). Once
231 formed, these tensile veins are widely overprinted by shearing events forming a zeolite-
232 cemented cataclasite/gouge with clasts of earlier zeolite vein material (Figs 5b, 7b).
233 Progressive shearing leads to the destruction of the vein clasts producing fine- to medium-
234 grained cataclasites (Figs 5b, 7c). The preservation of clasts of zeolite cataclasite suspended
235 in fine grained zeolite gouge also suggests that repeated shearing events have occurred along
236 some larger faults with many of these cataclasite clasts displaying well-developed haloes of
237 crystalline zeolite consistent with growth into a fluid-filled cavity (Fig. 7d). Following
238 cementation, many N-S and NNE-SSW shear fractures have also been reopened as tensile
239 fractures filled with new crystalline zeolite (Fig. 7e). E-W faults do not host widespread
240 tensile veins and tend to carry either zeolite mineralized cataclasite and gouge (e.g. Figs 2d,
241 3d), or to be clean breaks (e.g. Fig. 2f). One feature spatially associated with some larger E-
242 W faults (e.g. T1, T3) is the presence of zeolite gouge injections both into the host rocks
243 along sub-vertical N-S fractures and internally within fault zones cross-cutting earlier
244 gouges/cataclasites (Figs 6a-c, 7f).

245 In summary, the faults and fractures have clearly hosted significant aqueous fluid
246 flow during their history leading to the observed zeolite mineralization and alteration of the
247 immediately adjacent tonalite host rocks. They typically preserve a history of one or more
248 cycles of fracturing and cataclasis followed by cementation and sealing possibly related to
249 fluid pressure fluctuations during deformation. N-S and NNE-SSW structures carry
250 widespread tensile or hybrid veins fills that are either overprinted by later shearing or
251 reactivate pre-existing shear fractures.

252 *3.3. Evidence for seismogenic behaviour during formation of zeolite-bearing brittle* 253 *structures*

254 Petrographic, microstructural, geochemical and stable isotopic analyses (e.g.
255 Pennacchioni *et al.*, 2006; Smith *et al.* 2013; Mittemperger *et al.* 2014) have shown that the
256 first ingress of crustal metamorphic fluids in the Adamello Massif occurred *prior* to the
257 zeolite mineralization during dextral cataclastic faulting along the GLFZ. The widespread
258 preservation of pseudotachylytes associated with these E-W faults demonstrates the
259 repeatedly seismogenic nature of the fault zone at that time (e.g. see Di Toro & Pennacchioni
260 2004, 2005). Equivalent geological indicators of seismic slip (cf. Cowan 1999; Niemeijer *et*
261 *al.* 2012) are not associated with the zeolite-hosting fault movements. Nevertheless, there is
262 other geological evidence to suggest that at least some of the zeolite-bearing fault
263 displacements were seismogenic. Zeolite-mineralized gouge injections along N-S tensile
264 fractures are observed linking up into two of the largest E-W sinistral-reverse faults in the
265 area (T1, T3, see Figs 6a-c, f). Earthquake events can rapidly amplify fluid pressures along
266 faults for short time periods (e.g. Nur and Booker, 1972) leading to the fluidization and local
267 injection of unconsolidated fault gouges (e.g. see Sibson, 1993; Smith *et al.* 2008; Rowe *et al.*
268 2012). In the following section, we investigate the relationships between stress, variations in

269 fluid pressure and possible seismogenic slip to explain the observed kinematic diversity of
270 zeolite-bearing structures.

271

272 **4. Palaeostress analysis, fault reactivation potential and Coulomb stress modelling**

273 We analysed the reactivation potential of pre-existing structures with different orientations in
274 the Lobbia Glacier valley in three stages:

275 i) The slickenline data measured from the three different fault sets (NNE-SSW sinistral,
276 N-S normal and E-W sinistral-reverse) were used to infer the orientations of the principal
277 palaeo-stresses during the formation of the zeolite-bearing structures, using standard
278 stress inversion techniques (following Delvaux & Sperner, 2003, Fig. 9).

279 ii) The potential effects of elevated differential stresses and pore-fluid pressures on the
280 stability of reactivated structures were examined using a slip and dilation tendency
281 analysis (following Ferrill *et al.* 1999; Lisle & Srivastava 2004) (Fig 10a, b).

282 iii) Finally, we undertook Coulomb stress transfer modelling (following Lin & Stein
283 2004; Toda *et al.* 2005) to determine whether the observed kinematic diversity amongst
284 the zeolite-bearing structures can be explained by static loading (stress transfer) following
285 seismogenic slip along the main NNE-SSW sinistral structures.

286 *4.1. Palaeostress analysis*

287 Stress inversion techniques allow modelling of the stress tensor associated with a set
288 of coeval and consistent kinematic indicators (e.g. slickenlines) measured on a set of fault
289 surfaces. The fundamental assumption in all stress inversion techniques (Wallace, 1951; Bott,
290 1959) is the statistical parallelism between the observed slip vector (measured on fault
291 surfaces) and the model shear traction (shear component of stress tensor, resolved on a

292 particular fault plane via Cauchy's double dot product). This assumption is reasonable if the
293 fault displacements are small (infinitesimal strain and no rotation), a condition met by the
294 small-displacement zeolite-bearing structures considered here.

295 Several graphical and numerical approaches have been proposed (e.g. Angelier and
296 Mechler, 1977; Etchecopar *et al.*, 1981; Angelier, 1991; Michael, 1984; Reches, 1987;
297 Yamaji, 2000; Delvaux & Sperner, 2003). In most cases, the solution is obtained as a reduced
298 stress tensor with just four parameters (Etchecopar *et al.*, 1981): the orientation of the three
299 principal axes and the shape factor $\delta = (\sigma_2 - \sigma_3) / (\sigma_1 - \sigma_3)$. This tensor represents, in a-
300 dimensional form, the deviatoric component of the total stress tensor; the isotropic
301 component does not influence shear stress on fault surfaces. Ideally, the most robust
302 numerical solution requires at least four statistically independent fault sets to be measured
303 (see Angelier, 1991). In the case of the zeolite-bearing faults, this condition is met since we
304 have the three fault sets discussed above, plus a few faults in other scattered orientations.

305 Our modelling was performed using the Win Tensor software (Delvaux & Sperner,
306 2003). The inversion of the total zeolite-bearing fault and fracture dataset (Fig. 9) obtains a
307 wrench tectonic regime with σ_1 approximately horizontal N-S, σ_3 approximately horizontal
308 E-W, and σ_2 sub-vertical. The shape factor δ is 0.8, meaning that σ_2 is closer to σ_1 rather than
309 σ_3 . We also carried out analyses on smaller sub-sets of the total data located, for example,
310 inside and outside the GLFZ. This had little effect on either the nature or orientation of the
311 modelled principle stresses, leading us to conclude that despite the obvious scatter in
312 fault/fracture orientations (Fig. 9), the regional stress field at the time of faulting was
313 generally fairly consistent in orientation.

314 The Mohr circle plot showing the normal and tangential components of the stress
315 tensor resolved on each fault surface (Fig. 9) demonstrates that the NNE-SSW sinistral and

316 N-S normal faults are reasonably well oriented for slip as they fall in the hybrid
317 shear/opening field, while the E-W faults are strongly misoriented (Sibson, 1985b) since they
318 are characterized by high normal and low shear stresses. The plots also show that there are no
319 Andersonian faults in our datasets, a conclusion consistent with the field and microstructural
320 observations, which indicate that most brittle faults reactivate structures formed during
321 previous deformation phases.

322 The tectonic regime obtained from this analysis accords well with other results
323 obtained for this part of the Alps in the Miocene (17-7Ma, e.g. Prosser, 1998; Castellarin *et*
324 *al.*, 2006, Agliardi *et al.*, 2009), where the main regional-scale system is represented by the
325 NNE-SSW sinistral Giudicarie Fault System that lies to the east of the Adamello Massif (Fig.
326 1a; Prosser 1998; Viola *et al.* 2001). Similarly orientated brittle sinistral faults are also known
327 to offset exposed segments of the Tonale Fault by up to 600m (e.g. see figure 2 in Stipp *et al.*
328 2004). We therefore conclude that the zeolite-bearing fault structures in the Lobbia Glacier
329 valley belong to a regionally recognized late fault system of probable Miocene age.

330 4.2. Slip tendency and dilation tendency analyses

331 A slip and dilation tendency analysis is appropriate in the case of the zeolite-bearing
332 faults of the Lobbia Glacier valley since reactivation is almost invariably observed, meaning
333 that the pre-existing faults are likely to be significantly weaker than the intact tonalite. Slip
334 tendency (Morris *et al.*, 1996), and particularly normalized slip tendency (Lisle and
335 Srivastava, 2004), defined as $NST = \tau/\sigma_n/\mu$, (the shear to normal stress ratio on a given
336 fault or fracture surface, normalized by the friction coefficient) represents the proneness to
337 slip of that particular structure. Thus critically stressed Andersonian faults show $NST = 1$,
338 whilst surfaces parallel to a principal plane of the stress tensor, with zero shear stress, have
339 $NST = 0$ (Bistacchi *et al.*, 2012).

340 Dilation tendency is defined as $DT = (\sigma_1 - \sigma_n)/(\sigma_1 - \sigma_3)$, where σ_n is the normal
341 stress acting on a particular structure. This represents the proneness of a fracture with a given
342 orientation to open under an imposed fluid pressure (Ferrill *et al.*, 1999). In Figure 10a and b,
343 both NST and DT are colour-coded on the stereoplot for the proposed regional stress regime
344 (Fig. 9c), and poles corresponding to typical attitudes of NNE-SSW, N-S and E-W faults are
345 highlighted. In addition, the MATLAB[®] Toolbox of Bistacchi *et al.* (2012) allows the
346 prediction of the orientation of theoretical Andersonian surfaces, which are also shown.

347 The hypothetical Andersonian faults predicted by the analysis are not recognized in
348 the field. As a result of their high DT values, the NNE-SSW and N-S structures are likely to
349 open as soon as the fluid pressure overcomes σ_3 , and thus these structures are able to behave
350 as very effective preferential fluid circulation pathways. Once a fracture network or mesh is
351 established, fluid pressure can rise to higher levels, at least locally and episodically. The N-S
352 structures also have high NST values (despite being non-Andersonian), so they are the most
353 likely to be reactivated amongst the pre-existing structures. Conversely, the E-W faults have
354 low NST and DT values, and therefore require higher fluid pressure to be activated in slip,
355 and also to open and be infiltrated by fluids. Sub-vertical N-S veins show the highest DT
356 (almost 1), in agreement with the field and microstructural observations that these tensile
357 veins (e.g. Fig. 2b, 6b, c) are the only possible newly formed (as opposed to reactivated)
358 structures developed under these stress conditions. They potentially formed as tensile
359 hydraulic fractures when the fluid pressure exceeded σ_3 plus the tensional strength of the
360 intact tonalites.

361 4.3. Coulomb stress modelling

362 Following the pioneering studies of Reasenberg & Simpson (1992), King *et al.* (1994)
363 and Stein *et al.* (1997), it is now well known that the variable slip distribution on a fault

364 during an earthquake results in an heterogeneous strain field in the wall rocks. This in turn,
365 can produce elastic stresses that perturb the regional stress field, resulting in an increased or
366 decreased possibility of failure on nearby faults. Such a *stress transfer* process is now
367 commonly invoked in order to explain earthquake triggering (on already critically-loaded
368 faults) and might also plausibly play a role in the development of the zeolite-hosting fracture
369 systems of the Lobbia Glacier valley.

370 The longest and possibly largest displacement fault in the area is the NNE-SSW
371 trending sinistral structure located in the centre of the Lobbia Glacier valley (fault S1; Figs
372 1b, c). It shows a maximum sinistral offset of 5 metres (based on offset igneous markers)
373 close to the toe of the Lobbia Glacier, decreasing northwards to <2 metres where it offsets
374 fault T1 (Fig. 3f). Whilst the *ca.* 5 m offset may include displacements along pre-existing
375 sinistral mylonitic shear zones, the *ca.* 2 m offset of fault T1 can be confidently associated
376 with the zeolite-associated faulting episode (Fig. 4). Further to the north, fault S1 branches
377 into two zones of increasingly small offset, linked strike-slip and normal fault segments that
378 die out close to fault T4 (Fig. 1b). This overall northwards decrease in offset magnitude is
379 consistent with northward fault propagation of a fault tip zone. Using the methods of Lin &
380 Stein (2004), King *et al.* (1994) and Toda *et al.* (2005), we use the Coulomb 3.2 stress
381 modelling code within MATLAB[®] (<http://earthquake.usgs.gov/research/modeling/coulomb/>)
382 to estimate the static stress changes resulting from an hypothetical sinistral “mainshock”
383 rupture along fault S1.

384 Assuming a depth of 4 km, we model a single hypothetical rupture on the fault S1
385 approximately equivalent to an $M = 3$ earthquake (0.2 m maximum slip at the toe of the
386 Lobbia glacier in the south, tapering to 0 m at the northern tip of the fault). A slip scenario of
387 this kind results in a transient, localized near-field stress perturbation in the vicinity of the
388 fault (Fig. 11a). The distribution of stress concentrations generated by slip on S1 (represented

389 as Coulomb stress change resolved onto fault surfaces with the same orientation as the
390 reactivated E-W structures, taken as 100/50 S) matches well with the distribution of the
391 reactivated thrust segments observed in the field (Figs 11a,b). To test the resolved direction
392 of slip on E-W faults that could be triggered by rupture (or repeated ruptures) on S1, we
393 inserted 3 synthetic E-W faults (coincidental with T1, T2 and T3) and calculated the most
394 likely rake direction during failure. From this calculation the E-W faults would be expected
395 to fail with as sinistral-reverse faults with a rake of 55° (Fig. 11c) almost exactly matching
396 the slickenline lineations measured in the field (see Fig. 8). The stress transfer model also
397 explains the changes in damage zone thickness of the larger E-W faults such as fault T1,
398 which is up to 2 m adjacent the largest NNE-SSW fault, gradually decreasing to almost zero
399 250m along strike and away from the fault intersection (Fig. 4). Similar along-strike
400 variations in displacement can be also accommodated by secondary displacements along the
401 smaller N-S-trending normal faults located in the hangingwall regions of the E-W faults (Fig.
402 11d). Note that thrust and normal fault displacements would be necessarily limited since they
403 would have rapidly dissipated the local stress perturbation, and the system would have
404 reverted to the homogeneous far-field regional stress field in which the E-W structures were
405 once again stable.

406 The model presented in Figure 11a examines the stress transfer that could occur
407 during a single small rupture event along the fault S1. Given the field and microstructural
408 evidence for multiple fracture and associated mineralization episodes, it seems probable that
409 repeated rupturing events, each with a potential associated stress transfer will have occurred.
410 It is also possible that other large N-S faults (e.g. S2, S3) have hosted mainshock rupture
411 events at some time in their history. The preservation of injected gouges in the footwalls of
412 faults T1 and T3 suggests that once these faults were sufficiently loaded, they also failed
413 seismically, but we have chosen to not model the stress transfers associated with slip along

414 these E-W faults as we are unable to constrain their finite displacements due to a lack of
415 offset markers.

416 *4.4. Summary*

417 The analyses presented above suggest that reactivation of the pre-existing, generally
418 N-S-trending structures (NNW-SSE sinistral, N-S normal faults) within the inferred regional
419 stress field is plausible particularly when assisted by the development of elevated differential
420 stresses and/or pore-fluid pressures. The sinistral-reverse kinematics observed along the
421 zeolite-bearing E-W faults are consistent with the predictions of Coulomb stress transfer
422 following slip along the main N-S structures. In the following discussion, we address the
423 possible relationships between deformation, pore pressure variation and the timescales of
424 fracturing within the *ca.* 0.5 km³ rock volume surrounding the main N-S structures.

425

426 **5. Discussion**

427 *5.1. Changes in pore fluid pressure and stress*

428 The forgoing description and analyses show that in the area of the Lobbia Glacier
429 valley, a kinematically diverse set of coeval zeolite mineralised faults and veins with various
430 orientations are spatially associated with the upper part and immediate hangingwall of the
431 older GLFZ. The observed mineralization and associated alteration of the tonalite wall rocks
432 requires the ingress and throughput of significant volumes of aqueous, low temperature
433 (<200°C) alkaline fluids (see Weisenberger & Bucher 2010 and references therein). This
434 fluid flow has clearly been facilitated by brittle fracturing and fault reactivation. So how
435 might these processes be related?

436 It is well known that failure along faults may be driven by either increases in shear
437 stress during the seismic cycle (stress-driven faulting), or by increases in pore fluid pressure
438 leading to hydrofracture (hydraulically-driven faulting) or by some intermediate combination
439 of these end-member controls (e.g. Phillips 1972; Sibson 1981; Cox 2010). A key observation
440 made both in the field and thin section is that many N-S and NNE-SSW shear fractures also
441 opened periodically as tensile or hybrid fractures and veins (e.g. Figs 2b, 3a, 5a). This
442 requires the development of elevated fluid pressures and hydrofracturing on the reasonable
443 assumption that the zeolite-bearing fracture systems formed at depths > 1-2km (Cox 2010).

444 In a hydraulically-driven scenario where the differential stresses remain constant an
445 increase in pore fluid pressures will reduce all the effective compressive principal stresses by
446 an amount equal to the fluid pressure assuming that poro-elastic effects (Nur & Byerlee 1971)
447 are negligible. Mohr circles are translated to the left and can ultimately strike the failure
448 envelope leading to failure (e.g. see Twiss & Moores 1992; Zoback 2007; Jaeger *et al.* 2007).
449 The field and microstructural observations show that the formation of the majority of N-S and
450 NNE-SSW tensile fractures is typically followed by frictional sliding and cataclasis (shear
451 fracture) during either sinistral or normal fault movements on NNE-SSW and N-S trending
452 structures, respectively. It is self-evident that more modestly elevated pore fluid pressures
453 would be required in order for shear failure to occur along suitably oriented cohesionless
454 fractures.

455 It seems unlikely that changes in fluid pressure alone caused the observed fracturing
456 associated with the zeolite mineralization since this cannot explain how the unfavourably
457 oriented E-W structures were reactivated at the same time as the NNE-SSW and N-S
458 structures. Furthermore the recognition of tensile, hybrid and shear fracturing events along
459 the NNE-SSW and N-S structures points to variations in the magnitudes of the differential

460 stress with time. The possible relationships between stress-driven seismogenic faulting, fluid
461 flow and mineralization are now examined and discussed.

462 *5.2. Timescales for seismogenic faulting*

463 Our findings are consistent with an initial hypothesis that the geometric and kinematic
464 relationships preserved within the zeolite-bearing structures of the Lobbia Glacier valley
465 represent a plausible geological analogue for foreshock-aftershock sequence and/or
466 earthquake swarm complexity. Several examples of natural earthquake swarms and/or
467 foreshock-aftershock sequences have been ascribed to the presence and/or migration of pore
468 fluids or magma under elevated pressures. Miller *et al.* (2004), for example, describe an
469 example from the Umbria-Marche region of the northern Apennines in Italy where an
470 aftershock sequence was interpreted to have been triggered by the presence of elevated pore
471 fluid (CO₂) pressures at depth which led to the failure of apparently stable, moderately-
472 dipping normal faults. Rupture of this fault system is considered to have allowed the over-
473 pressured fluid to move progressively up-dip, destabilizing individual fault segments as it
474 migrated. This migration and the failures it induced were recorded as a complex sequence of
475 migrating aftershocks. Such earthquake clusters are often characterised by multiple seismic
476 events closely spaced in time and location, with highly variable earthquake focal
477 mechanisms, especially for the smaller events (e.g. Mogi, 1963; Scholz, 2002; Shearer *et al.*
478 2003; Kassaras *et al.*, 2014). There are also many examples of similarly complex induced
479 seismicity resulting from human activities where fluids have been injected into the crust
480 during shale-gas exploration, geo-sequestration or enhanced geothermal exploitation (e.g.
481 Raleigh *et al.*, 1976; Seeber *et al.*, 2004; Deichmann & Giardini, 2009; Baisch *et al.*, 2006;).
482 A key question, therefore, is to assess whether pore pressure diffusion through the *ca.* 0.5
483 km³ rock volume cut by kinematically-diverse zeolite-bearing structures in the Adamello
484 Massif is consistent with the timescales associated typical earthquake foreshock, aftershock

485 or swarm sequences. We use the mainshock model along the NNE-SSW-striking sinistral
486 fault to test whether an increase in pore fluid pressure generated in the immediate vicinity of
487 a rupture would be able to diffuse out through a fracture system over the timescales of a
488 typical aftershock sequence.

489 The timescale, τ , for any diffusive process is given by:

$$490 \quad \tau = \frac{l^2}{\kappa} = \frac{(\phi\beta_f + \beta_r)\eta l^2}{k}, \quad (3)$$

491 where l = diffusion distance; κ = hydraulic diffusivity; ϕ = porosity; β_f = fluid
492 compressibility; β_r = rock compressibility; η = fluid viscosity; k = permeability (e.g.
493 Townend and Zoback, 2000; Wibberley, 2002). The studied zeolite-bearing structures seem
494 to cluster within *ca.* 0.5 km³ of the main NNE-SSW trending sinistral fault (Fig. 1b),
495 implying that a diffusion distance \leq 1000 m is appropriate. Figure 12 shows the timescales
496 for a pore pressure anomaly to diffuse distances between 100 and 10000 m, assuming a range
497 of hydraulic diffusivities κ . Clearly there is a large (*ca.* 7 orders of magnitude) variation in
498 reported or estimated hydraulic diffusivities. However, given the small displacements
499 observed along the zeolite-bearing faults in this part of the Adamello massif we suggest the
500 most appropriate diffusivity values to use here are those derived from: (1) static permeability
501 measurements of small (< 1 m) displacement, zeolite-bearing faults in crystalline basalt
502 (Walker *et al.*, 2013a, b); and (2) estimated *in situ* permeabilities for intraplate crust
503 (Townend and Zoback, 2000). These hydraulic diffusivities lie within the range 0.02 to 0.2
504 m²s⁻¹, giving characteristic diffusion timescales of 13 to 6600 days (0.04 to 18 years) over a
505 distance of 0.5 to 1 km (Fig. 12). Although imprecise – and adopting a steady, constant
506 hydraulic diffusivity is a significant over-simplification – the timescales associated with
507 hydraulic diffusivities toward the upper end of this range are consistent the timescales

508 associated with aftershock or other temporally-clustered earthquake events likely to have
509 been significantly influenced by fluid diffusion (e.g. Chen *et al.* 2012).

510 5.3. Fluid influx and cyclic reactivation model

511 The analyses presented above demonstrate that the brittle reactivation of a cluster of
512 differently oriented pre-existing structures and the associated zeolite mineralisation can be
513 explained by seismogenic fracturing processes in the presence of an at least locally
514 overpressured fluid in the Adamello Massif. In the following section, we propose a highly
515 simplified conceptual model.

516 *i) Initial fluid ingress:* The detailed study of fracturing associated with the dextral GLFZ
517 carried out by Smith *et al.* (2013) suggests that, prior to zeolite mineralization, the rocks of
518 the Adamello Massif adjacent to and especially within the GLFZ were likely to have been
519 impermeable. These authors have documented pervasive fluid-rock interaction leading to
520 development of a 200m thick zone of K-feldspar-epidote-chlorite alteration and veining
521 centred on the core of the GLFZ (Fig. 1b). Up to 85% of the observed microfractures in this
522 zone are sealed by these minerals.

523 In order to introduce the zeolite-mineralizing fluid required by our field and
524 microstructural observations, we follow Yardley (1997) in suggesting that the fluid pressure
525 in the low permeability tonalities was initially sub-hydrostatic. Mineralising fluids must have
526 been drawn into these crystalline rocks by early tectonically-induced rupturing along deeply
527 penetrating brittle fractures such as the larger displacement NNE-SSW sinistral fault set (Fig.
528 13). If early zeolite mineralisation followed initial fluid ingress, this would trap fluids and
529 promote the development of fluid overpressures within the fractures (cf. Sleep & Blanpied
530 1992). It also seems likely that the steeply south-dipping, pre-existing alteration zone centred
531 on the GLFZ would have acted as an impermeable barrier helping to further trap and

532 overpressure the zeolite-bearing fluids. Given the observed preferential development of this
533 mineralisation in the immediate hangingwall and upper part of the GLFZ, we suggest that the
534 fluids may have been drawn either vertically down or laterally from the south into position.
535 This proposal could plausibly be tested using stable isotopic analyses to test whether the
536 fluids associated with mineralization have a meteoric signal consistent with derivation from a
537 near surface source.

538 *ii) Cyclic seismogenic faulting, fluid-assisted rupturing and mineralisation:* we propose that a
539 series of “mainshock” ruptures occurred along one or more of the large NNE-SSW sinistral
540 faults – such as fault S1 (Figs 13i,iv,vii) leading to an increase in pore fluid pressure in the
541 upper part of the GLFZ immediately adjacent to the pre-existing impermeable zone of
542 alteration. We suggest that fluid migration and/or pressure diffusion away from the main
543 rupture transiently led to increases in local pore fluid pressure (Figs 13ii, v, viii). Depending
544 on the state of differential stress, this could have led to aftershock slip events due to hydraulic
545 tensile/hybrid fracturing (low differential stress) or to hydraulically-assisted shear fracturing
546 (high differential stress) along pre-existing NNE-SSW strike-slip and N-S normal faults (Figs
547 13ii, v, viii). Multiple mainshock rupturing events would also lead to stress transfer and
548 periodic partial reactivation of the adjacent E-W faults in the GLFZ. Following each
549 mainshock rupture, differential stresses and perhaps pore fluid pressures would likely fall,
550 meaning that the majority of the pre-existing structures once again became stable. Any
551 decrease in pore fluid pressure would also lead to zeolite precipitation (Figs 13iii, vi, ix). This
552 would effectively seal the faults and allow elevated fluid pressures to begin to develop again
553 either due to further influx of fluids and/or due to repeated seismic mainshocks along the
554 larger NNE-SSW fault(s) re-starting the rupture-reactivation-cementation cycle (Figs 13i-iii,
555 iv-vi, vii-ix; cf. Sibson et al. 1995).

556 It is not unreasonable to suggest that every fracture-forming event in crystalline rocks
557 of the Adamello Massif had the capacity to produce a small earthquake, be it a stress- or
558 fluid-driven process. Having produced a model to account for the spatial and temporal
559 clustering of fractures in the *ca.* 0.5 km³ of rock located close to the GLFZ in the Lobbia
560 Glacier valley, we used MyFault™ software to generate synthetic earthquake focal
561 mechanisms for illustrative purposes, using fault surfaces as principal nodal planes and
562 kinematic data to reconstruct the auxiliary plane.

563 Using the deformation sequence described in this paper and the synthetic earthquake
564 focal mechanisms, Figures 13i-ix schematically illustrate a hypothetical aftershock sequence
565 leading to reactivation of the zeolite-hosting structures in the Adamello Massif. Note that the
566 relative magnitudes of the aftershocks shown are purely schematic as these are unconstrained.
567 For instance, both the NNE-SSE striking faults and the E-W faults given their dimensions
568 could produce the main shocks of an earthquake sequence hosted in the investigated rock
569 volume. However, the field evidence discussed earlier suggests that the NNE-SSW faults
570 hosted the main (sinistral strike-slip) seismic ruptures. It is these faults that were most
571 favourably oriented with respect to the inferred late Miocene regional stress tensor of this
572 sector of the Southern Alps. As a consequence, though seismic faulting occurred along strike-
573 slip, normal and transpressive faults in the area, only the major ruptures were consistent with
574 the regional stress. This is similar to many foreshock/mainshock/aftershock sequences and
575 swarms. For instance, in the case of the 2011 Oichalia (Greece) swarm, the main shocks ($3 <$
576 $M_w < 4.8$) have focal mechanism (normal) consistent with the stress field (extensional) of the
577 area (Kassaras *et al.*, 2014). By contrast, the few interpretable focal mechanisms of the
578 smaller earthquakes ($M_w < 3$) are scattered, and include strike-slip and reverse mechanisms.
579 The evolution of this swarm was probably controlled by fluid migration along the main
580 extensional structures (Kassaras *et al.*, 2014). In general, normal faults and strike-slip faults

581 are more permeable given their lower mean stress allowing fluid ingress, which then
582 significantly influences the earthquake sequence evolution.

583 The sequence we describe is also comparable to the earthquake sequence observed in
584 New Madrid in 1811-1812 (Mueller *et al.*, 2004) albeit on different length scales. Here
585 rupture on the NE trending Cottonwood Grove Fault (dextral strike-slip) led to stress-loading
586 upon and subsequent failure of the SW-dipping Reelfoot Thrust. Our modelled earthquake
587 swarm shows a spatially distributed and complex mixture of focal mechanisms that is also
588 similar to the cloud of focal mechanisms observed for the more recent (1974-2006) micro-
589 seismicity in the New Madrid region (Mueller *et al.*, 2004; Shumway, 2008).

590

591 **6. Conclusions**

592 1) Small displacement late brittle fractures hosting zeolite mineralisation form a diffuse array
593 of structures in the upper part and immediate hangingwall of the GLFZ in the Lobbia Glacier
594 valley. Formed due to the ingress of aqueous alkaline fluids at <200°C, and at depths of 2.5-
595 6 km, we have shown that the locations and geometries of the mineralized fractures are
596 controlled by the distributed presence of pre-existing structures formed during the earlier
597 history of the Adamello pluton and GLFZ.

598 2) Geological observations and stress analyses suggest that favourably orientated pre-existing
599 NNE-SSW and N-S structures were initially reactivated under stress loading and/or
600 transiently high pore fluid pressure conditions developed adjacent to a pre-existing highly
601 cemented low permeability barrier located in the core of the GLFZ. Once formed, these
602 fractures were then susceptible to repeated reactivation as both shear and tensile fractures.

603 3) Coulomb stress modelling shows that repeated fluid-assisted seismogenic rupturing along
604 the main NNE-SSW sinistral fault(s) plausibly led to stress transfer and loading of previously
605 stable pre-existing E-W structures of the GLFZ which were reactivated as sinistral-reverse
606 faults. Seismogenic movements induced localised fluid over-pressurization leading to further
607 tensile fracturing and injection of fluidized zeolite-bearing gouges. The interaction between
608 the NNE-SSW sinistral faults and E-W sinistral-reverse faults also may have led to further
609 accommodation movements along linked N-S trending normal faults.

610 4) Decreases in stress and/or pore fluid pressures following rupture events and the formation
611 of fracture meshes appear to have led to system locking and cementation by zeolite
612 mineralization. This would have reduced the efficiency of fluid migration, allowing elevated
613 fluid pressures to be re-established thus helping to restart the “rupture-reativation-
614 cementation” cycle.

615 5) We propose that the reactivated mineralized structures associated with the GLFZ represent
616 a vivid geological manifestation of multiple ancient earthquake clusters – perhaps a series of
617 mainshock-aftershock events (as illustrated schematically in Figure 13). Their kinematic
618 complexity is clearly shown to result from the reactivation of pre-existing structures in a wide
619 range of orientations.

620 6) Our findings illustrate the importance of fluids and reactivation in upper crustal
621 seismogenic faulting processes and provide useful geological constraints that allow a better
622 understanding of the complex geological manifestations of natural earthquakes at depth.

623

624 **Acknowledgements:** The authors would like to thank Tom Mitchell, Jean Pierre Gratier,
625 Steve Smith, Silvia Mittempergher, Angela Castagna, Marieke Rempe, Marie Violay,
626 Michele Fondriest, Andrea Zanchi, Matteo Massironi and, Nicola DePaola for discussions
627 and help during fieldwork. Federico Zorzi is thanked for XRD analysis and Leonardo Tauro

628 and Elena Masiero for thin section preparation. The financial and scientific support of the
629 Leverhulme Trust (to Holdsworth), Durham University and of the European Research
630 Council Starting Grant USEMS No. 205175 (to Di Toro) are warmly acknowledged. Stephen
631 Cox, Andrea Billi, Steve Micklethwaite and Anonymous are thanked for their reviewers
632 comments. Stress inversion was performed with Win Tensor, courtesy of Damien Delvaux
633 (<http://www.damiendelvaux.be/Tensor/WinTensor/win-tensor.html>). Coulomb stress
634 modelling was performed using “Coulomb 3” software, courtesy of USGS and partners
635 (<http://earthquake.usgs.gov/research/modeling/coulomb/>).

636

637 **References**

638 Agliardi, F., Zanchi, A., Crosta, G.B., 2009. Tectonic vs. gravitational morphostructures in
639 the central Eastern Alps (Italy): Constraints on the recent evolution of the mountain range.
640 *Tectonophysics* **474**, 250–270. Anderson, E. M. 1951. *The Dynamics of Faulting*. (2nd Edn)
641 Oliver & Boyd, Edinburgh.

642

643 Angelier, J., 1991. Inversion directe de recherche 4-D: comparaison physique et
644 mathématique de deux méthodes de détermination des tenseurs des paléocontraintes en
645 tectonique de failles. *Compte Rendus l'Académie des Sci. Paris* **312**, 1213–1218.

646

647 Angelier, J., Mechler P., 1977. Sur une méthode graphique de recherche des contraintes
648 principale également utilisable en tectonique et en seismologie: la méthode des dièdres droits.
649 *Bulletin de la Société Géologique de France*, **7**, 1309-1318.

650

651 Baisch, S., Weidler, R. Voros, R., Wyborn, D., de Graaf, L. 2006, Induced Seismicity during
652 the Stimulation of a Geothermal HFR Reservoir in the Cooper Basin, Australia, *Bulletin of the*
653 *Seismological Society of America*, **96(6)**, 2242-2256.

654

655 Bestmann M., Pennacchioni G., Nielsen S., Göken M., de Wall H. 2012. Deformation and
656 ultrafine dynamic recrystallization of quartz in pseudotachylyte-bearing brittle faults: A
657 matter of a few seconds. *Journal of Structural Geology*, **38**, 21-38.

658

659 Bianchi A., Dal Piaz, G.B. 1937. Atlante geologico-petrografico dell'Adamello meridionale;
660 regione fra lo Stabio ed il Caffaro. *Mem. Ist. Geol. Min. Univ. Padova*, **12**, 1–16.

661

662 Bianchi A., Callegari, E., Jobstraibizer, P.G. 1970. I tipi petrografici fondamentali del plutone
663 dell'Adamello (tonaliti, quarzodioriti, granodioriti e loro varietà leucocrate).*Mem. Ist. Geol.*
664 *Min. Univ. Padova*, **27**,1–148.

665

666 Bistacchi, A., Massironi, M, Menegon, L., Bolognesi, F., Dongi,V. 2012. On the nucleation
667 of non-Andersonian faults along phyllosilicate-rich mylonite belts. In: Healy, D., Butler, R.
668 W. H., Shipton, Z. K. & Sibson, R. H. (eds) *Faulting, Fracturing and Igneous Intrusion in*
669 *the Earth's Crust*. Geological Society, London, Special Publications, **367**, 185–199.
670 [http://dx.doi.org/ 10.1144/SP367.13](http://dx.doi.org/10.1144/SP367.13)

671

672 Bott, M.H.P., 1959. The mechanisms of oblique slip faulting. *Geological Magazine*, **96**, 109–
673 117.

674

675 Brack, P., 1981. *Structures in the southwestern border of the Adamello intrusion*.
676 *Schweizerische Mineralogische und Petrographische Mitteilungen* 61, 37–50.

677

678 Callegari E. 1985. *Geological and petrological aspects of the magmatic activity at Adamello*
679 *(northern Italy)* *Memorie della Società Geologica Italiana*, **26**, 83–103

680

681 Callegari E., Brack P. 2002. *Geological map of the Tertiary Adamello batholith (Northern*
682 *Italy) -Explanatory notes and legend*. *Memorie di Scienze Geologiche*, **54**, 19–49

683

684 Castellarin, A., Vai, G.B., Cantelli, L., 2006. The Alpine evolution of the Southern Alps
685 around the Giudicarie faults: A Late Cretaceous to Early Eocene transfer zone.
686 *Tectonophysics* **414**, 203–223.

687

688 Chen, X., Shearer, P.M., Abercrombie, R.E., 2012. Spatial migration of earthquakes within
689 seismic clusters in Southern California: Evidence for fluid diffusion, *Journal of Geophysical*
690 *Research*, **117**, doi: 10.1029/2011JB008973.

691

692 Chung, F.H. (1974) Quantitative interpretation of X-ray diffraction patterns of mixtures. II.
693 Adiabatic principle of X-ray diffraction analysis of mixtures. *Journal of Applied*
694 *Crystallography*, **7**, 526–531.

695

696 Collettini C., Trippetta F 2007. A slip tendency analysis to test mechanical and structural
697 control on aftershock rupture planes. *Earth and Planetary Science Letters*, **255**; 402-413, doi:
698 10.1016/j.epsl.2007.01.001.

699

700 Collettini C., Holdsworth R.E., Smith S.A.F. 2009. Fault Zone Structure and Deformation
701 Processes along an Exhumed Low-Angle Normal Fault: Implications for Seismic Behaviour
702 Review Article. *International Geophysics*, **94**, 69-85

703

704 Cowan, D.S., 1999, Do faults preserve a record of seismic slip? A field geologist's opinion:
705 *Journal of Structural Geology*, **21**, 995-1001.

706

707 Cox, S.F. 1987. Antitaxial crack-seal vein microstructures and their relationship to
708 displacement paths. *Journal of Structural Geology*, **9**, 779-787.

709

710 Cox, S.F. 2010. The application of failure mode diagrams for exploring the roles of fluid
711 pressure and stress states in controlling styles of fracture-controlled permeability
712 enhancement in faults and shear zones. *Geofluids*, **10**, 217–233, doi: 10.1111/j.1468-
713 8123.2010.00281.x

714

715 Deer, W.A., Howie, R.A., Zussman, J., 1992. *An Introduction to the Rock-Forming Minerals*.
716 Longman, Harlow.

717

718 Deichmann, N., D. Giardini, 2009, Earthquakes Induced by the Stimulation of an Enhanced
719 Geothermal System below Basel, Switzerland, *Seismological Research. Letters*, **80**, 784-798.

720

721 Del Moro A., Pardini, G. Quercioli, C., Villa, I.M., Callegari, E. 1983. *Rb/Sr and K/Ar*
722 *chronology of Adamello granitoids, Southern Alps*. *Memoir Società Geologica Italiana*, **26**,
723 285–299

724

725 Delvaux, D., Sperner B., 2003. New aspects of tectonic stress inversion with reference to the
726 TENSOR program. In: D.A. Nieuwland (ed.), *New Insights into Structural Interpretation and*
727 *Modelling*, Geological Society, London, Special Publications, **212**, 75-100.

728

729 Di Toro, G., Pennacchioni, G., 2004. Superheated friction-induced melts in zoned
730 pseudotachylytes within the Adamello tonalites (Italian Southern Alps). *Journal of Structural*
731 *Geology*, **26**, 1783-1801.

732

733 Di Toro, G., Pennacchioni, G., 2005. Fault plane processes and mesoscopic structure of a
734 strong-type seismogenic fault in tonalites (Adamello batholith, Southern Alps).
735 *Tectonophysics*, **402**, 54-79

736

737 Etchecopar, A., Vasseur, G., Daignières, M., 1981. An inverse problem in microtectonics for
738 the determination of stress tensors from fault striation analyses. *Journal of Structural*
739 *Geology*, **31**, 51–65.

740

741 Ferrill, D.A., Winterle, J., Wittmeyer, G., Sims, D., Colton, S., Argmstrong, A., Morris, A.P.,
742 1999. Stressed rock strains groundwater at Yucca Mountain, Nevada. *GSA Today*, 9, 1–8.

743

744 Fischer, T., Horálek J., Hrubcová, P., Vavryčuk, V., Bräuer, K., Kämpf, H. 2013. Intra-
745 continental earthquake swarms in West-Bohemia and Vogtland: A review. *Tectonophysics*,
746 <http://dx.doi.org/10.1016/j.tecto.2013.11.001>

747

748 Hansmann A. W., Oberli, F. 1991. Zircon inheritance in an igneous rock suite from the
749 southern Adamello batholith (Italian Alps). *Contributions to Mineralogy and Petrology*, **107**,
750 501–518.

751

752 Godano, M., Larroque, C., Bertrand, E., Courboux, F., Deschamps, A., Salichon, J., Bland-
753 Guerry, C., Fourteau, L., Charléty, J. Deshayes, P. 2013. The October–November 2010
754 earthquake swarm near Sampeyre (Piedmont region, Italy): A complex multicluster sequence,
755 *Tectonophysics*, **608**, 97-111, dx.doi.org/10.1016/j.tecto.2013.10.010.

756

757 Hilgers C., Urai J. L. 2005. On the arrangement of solid inclusions in fibrous veins and the
758 role of the crack-seal mechanism. *Journal of Structural Geology*, **27**, 481-494.

759

760 Jaeger J.C., Cook N.G.W., Zimmerman R.W. 2007. *Fundamentals of Rock Mechanics* (4th
761 edition) Blackwell Publishing, pp 475.

762

763 Kassaras, I., Kapetanidis, V., Karakonstantis, A., Kouskouna, V., Ganas, A., Chouliaras, G.
764 Drakatos G., Moshou, A., Mitropoulou, V., Argyrakis, P., Lekkas, E., Makropoulos, K. 2014.
765 Constraints on the dynamics and spatio-temporal evolution of the 2011 Oichalia seismic
766 swarm (SW Peloponnesus, Greece) *Tectonophysics*, 614, 100–127; doi:
767 10.1016/j.tecto.2013.12.012
768
769 King, G.C.P., Stein, R.S., Lin, J., 1994. Static stress changes and the triggering of
770 earthquakes, *Bulletin of the Seismological Society of America*, **84**, 935-953.
771
772 Kirkpatrick, J. D., Z. K. Shipton, J. P. Evans, S. Micklethwaite, S. J. Lim, and P. McKillop
773 2008, Strike-slip fault terminations at seismogenic depths: The structure and kinematics of
774 the Glacier Lakes fault, Sierra Nevada United States, *Journal of Geophysical Research*, **113**,
775 B04304, doi:10.1029/2007JB005311.
776
777 Kisslinger, C., 1975. Processes during the Matsushiro swarm as revealed by levelling,
778 gravity, and spring-flow observations, *Geology*, **3**, 57–62.
779
780 Lin, J., and Stein, R.S., 2004, Stress triggering in thrust and subduction earthquakes, and
781 stress interaction between the southern San Andreas and nearby thrust and strike-slip faults:
782 *Journal of Geophysical Research*, 109, B02303, doi:10.1029/2003JB002607.
783
784 Lisle, R.J., and Srivastava, D.C., 2004, Test of the frictional reactivation theory for faults and
785 validity of fault-slip analysis: *Geology*, **32**, 569-72.
786
787 Main, I.G., 1996. Statistical physics, seismogenesis, and seismic hazard. *Reviews of*
788 *Geophysics*, 34, 433–462.
789
790 Mayer A., Cortiana, G., Dal Piaz, G.V., Deloule, E., De Pieri, R., Jobstraibizer, P. 2003. U–
791 Pb single zircon ages of the Adamello batholith, Southern Alps. *Memoir Società Geologica*
792 *Italiana*, **55**, 151–167.
793
794 Michael, A.J., 1984. Determination of stress from slip data: faults and folds. *Journal of*
795 *Geophysical Research*, 89, 11517-11526.
796

797 Micklethwaite, S., Cox, S. F. 2004. Fault-segment rupture, aftershock-zone fluid flow, and
798 mineralization. *Geology*, **32**, 813-816.
799

800 Miller S. A., Collettini C., Chiaraluce L., Cocco M., Barchi M. & Kaus B. J. P. 2004.
801 Aftershocks driven by a high pressure CO₂ source at depth. *Nature*, **427**,724-727.
802

803 Mittempergher, S., Pennacchioni,G., Di Toro, G. 2009. The effects of fault orientation and
804 fluid infiltration on fault rock assemblages at seismogenic depths. *Journal of Structural*
805 *Geology*, **31**, 1511-1524.
806

807 Mittempergher, S., Dallai, L. Pennachioni, G., Renard, F., Di Toro, G. 2014. Origin of
808 hydrous fluids at seismogenic depth: constraints from natural and experimental fault rocks,
809 *Earth and Planetary Science Letters*, **385**, 97-109.
810

811 Mogi K. 1963. Some discussions of aftershocks, foreshocks and earthquakes swarms –the
812 fracture of a semi-infinite body caused by an inner stress origin and its relation to earthquake
813 phenomena. *Bulletin of the Earthquake Research Institute*, **41**, 615–658.
814

815 Morris, A.P., Ferrill, D.A., Henderson, D.B., 1996. Slip tendency and fault reactivation.
816 *Geology*, **24**, 275–278.
817

818 Mueller K, Hough S. E., Bilham R., 2004. Analysing the 1811–1812 New Madrid
819 earthquakes with recent instrumentally recorded aftershocks. *Nature*, **429**, 284-288.
820

821 Niemeijer, A., Di Toro, G., Griffith, W.A., Bistacchi, A., Smith, S. a. F., Nielsen, S., 2012.
822 Inferring earthquake physics and chemistry using an integrated field and laboratory approach.
823 *Journal of Structural Geology*, **39**, 2–36.
824

825 Noir, J., Jacques, E., Bekri, S., Adler, P.M., Tapponnier, P. & King, G.C.P., 1997. Fluid flow
826 triggered migration of events in the 1989 Dobi earthquake sequence of Central Afar,
827 *Geophysics Research Letters*, **24**, 2335–2338.
828

829 Nur, A., Booker, J.R., 1972. Aftershocks caused by pore fluid flow? *Science*, **175**, 885-887.
830

831 Nur, A., Byerlee, J.D. 1971. An exact effective stress law for elastic deformation of rock with
832 fluids. *Journal of Geophysical Research*, **76**, 6414-6419.
833

834 Pennacchioni G., Di Toro, G., Brack, P., Menegon, L., Villa, I.M. 2006. Brittle–ductile–
835 brittle deformation during cooling of tonalite (Adamello, Southern Italian Alps),
836 *Tectonophysics*, **427**, 171-197
837

838 Phillips, W.J. 1972. Hydraulic fracturing and mineralisation. *Journal of the Geological*
839 *Society of London*, **128**, 337-359.
840

841 Prosser, G. 1998. Strike-slip movements and thrusting along a transpressive fault zone: The
842 North Giudicarie line (Insubric line, northern Italy). *Tectonics*, **17**, 921–937.
843

844 Raleigh, C.B., Healy, J.H, Bredehoeft, J.D. 1976, An Experiment in Earthquake Control at
845 Rangely, Colorado, *Science*, **191**, 1230-1237.
846

847 Reasenberg, P.A., Simpson, R.W. 1992. Response of regional seismicity to the static stress
848 change produced by the Loma Prieta earthquake. *Science*, **255**, 1687-1690.
849

850 Reches, Z., 1987. Determination of the tectonic stress tensor from slip along faults that obey
851 the Coulomb yield condition. *Tectonics*, **6**, 849–861.
852

853 Reverman R.L., Fellin M.G., Herman F., Willett S.D., Fitoussi C., 2012. Climatically versus
854 tectonically forced erosion in the Alps: Thermochronometric constraints from the Adamello
855 Complex, Southern Alps, Italy. *Earth and Planetary Science Letters*, **339**, 127-138.
856

857 Rowe, C. D., Kirkpatrick, J. D. and Brodsky, E. E. 2012. Fault rock injections record paleo-
858 earthquakes. *Earth and Planetary Science Letters*, **335-336**, 154-166.
859

860 Scholz C.H. 2002. *The Mechanics of Earthquakes and Faulting*. Cambridge University Press,
861 New York, pp 439.
862

863 Seeber, L., Armbruster, J.G. and Kim, Y.K. 2004. A Fluid-Injection Earthquake Sequence in
864 Ashtabula, Ohio: Implications for Seismogenesis in Stable Continental Regions, *Bulletin of*
865 *the Seismological Society of America*, **94**, 76-87.

866

867 Shapiro, S.A., Rentsch, S., Rothert, E., 2005. Characterization of hydraulic properties of
868 rocks using probability of fluid-induced microearthquakes. *Geophysics*, **70**, F27-F33.

869

870 Shearer, P.M., Hardebeck, J.L., Astiz, L., Richards-Dinger, K.B. 2003. Analysis of similar
871 event clusters in aftershocks of the 1994 Northridge, California, Earthquake. *Journal of*
872 *Geophysical Research*, 108 (B1) 2035, doi: 10.1029/2001JB000685.

873

874 Shumway A. M., 2008. Focal Mechanisms in the Northeast New Madrid Seismic Zone.
875 *Seismological Research Letters*. **79**, 469-477.

876

877 Sibson, R.H. 1981. Fluid flow accompanying faulting: field evidence and models. In:
878 Simpson, D. W., Richards, P.G., (eds.). *Earthquake Prediction: an International Review*.
879 Maurice Ewing Series 4, American Geophysical Union, Washington D.C., 593-603.

880

881 Sibson R.H. 1985a, Stopping of earthquake ruptures at dilational fault jogs: *Nature*, **316**, 248-
882 251.

883

884 Sibson, R.H., 1985b. A note on fault reactivation. *Journal of Structural Geology*, **7**, 751-754.

885

886 Sibson, R. H. 1993. Load-strengthening versus load-weakening faulting. *Journal of*
887 *Structural Geology*, **15**, 123-128.

888

889 Sibson, R. H. 1995. Structural permeability and fluid flow in fault-fracture meshes. In: Mauk,
890 J. L., St George, J. D. (eds). *Proceedings of the 1995 PACRIM Congress, Auckland, New*
891 *Zealand, 19-22 November 1995*. The Australasian Institute of Mining and Metallurgy
892 Publication Series **9/95**, 521-526.

893

894 Sibson R.H., Robert F., Poulsen K.H. 1988. High-angle reverse faults, fluid-pressure cycling
895 and mesothermal gold-quartz deposits. *Geology*, **16**, 551-55.

896

897 Sleep, N. H., Blanpied, M. L., 1992, Creep, compaction and the weak rheology of major
898 faults, *Nature*, **359**, 687-692.

899 Smith S.A.F., Collettini C., Holdsworth R.E. 2008. Recognizing the seismic cycle along
900 ancient faults: CO₂-induced fluidization of breccias in the footwall of a sealing low-angle
901 normal fault. *Journal of Structural Geology*, **30**, 1034-1046.

902

903 Smith, S.A.F., Bistacchi, A., Mitchell, T., Mittempergher, S., DiToro, G., 2013. The structure
904 of an intraplate exhumed seismogenic fault in crystalline basement. *Tectonophysics*, **599**, 29–
905 44.

906

907 Stein R.S. Barka A.A. Dieterich, J.H. 1997. Progressive failure on the North Anatolian fault
908 since 1939 by earthquake stress triggering. *Geophysical Journal International*, **128**: 594-604.

909

910 Stipp M., B. Fügenschuh, L.P. Gromet, H. Stünitz & S.M. Schmid, 2004. Contemporaneous
911 plutonism & strike-slip faulting: a case study from the Tonale fault zone north of the
912 Adamello pluton (Italian Alps). *Tectonics*, **23**, p. TC3004.

913

914 Sykes, L. R. 1978. Intraplate seismicity, reactivation of preexisting zones of weakness,
915 alkaline magmatism and other tectonism postdating continental fragmentation. *Reviews of*
916 *Geophysics and Space Physics*, **16**, 621-88.

917

918 Toda, S., Stein, R.S., Richards-Dinger, K., and Bozkurt, S., 2005, Forecasting the evolution
919 of seismicity in southern California—animations built on earthquake stress transfer: *Journal*
920 *of Geophysical Research*, 110, B05S16, doi:10.1029/2004JB003415.

921

922 Townend, J., and Zoback, M.D. 2000. How faulting keeps the crust strong, *Geology*, **28**, 399-
923 402.

924

925 Twiss R. J., Moores E. M. 1992. *Structural Geology*. W.H. Freeman & Company, pp.

926

927 Viola G., N.S. Mancktelow & D. Seward. 2001. Late Oligocene–Neogene evolution of
928 Europe–Adria collision: new structural & geochronological evidence from the Giudicarie
929 fault system (Italian Eastern Alps). *Tectonics*, **20**, 999–1020.

930

931 Wallace, R.E., 1951. Geometry of shearing stress and relation to faulting. *Journal of*
932 *Geology*, **59**, 118–130.

933

934 Walker, R.J., Holdsworth, R.E., Armitage, P.J., Faulkner, D.R., 2013a. Fault zone
935 permeability structure evolution in basalts, *Geology*, **41**, 59-62.

936

937 Walker, R.J., Holdsworth, R.E., Imber, J., Faulkner, D.R., Armitage, P.J., 2013b. Fault zone
938 architecture and fluid flow in interlayered basaltic volcanoclastic-crystalline sequences,
939 *Journal of Structural Geology*, **51**, 92–104.

940

941 Wibberley, C.A.J., 2002. Hydraulic diffusivity of fault gouges and implications for thermal
942 pressurization during seismic slip. *Earth, Planets Space*, **54**, 1153-1171.

943

944 Weisenberger, T., Bucher, K. 2010. Zeolites in fissures of granites and gneisses of the Central
945 Alps. *Journal of Metamorphic Geology*, **28**, 825-847.

946

947 Weisenberger T.B., Rahn M. van der Lelji R., Spikings R. & Bucher K. 2012. Timing of
948 low-temperature mineral formation during exhumation and cooling in the Central Alps,
949 Switzerland. *Earth and Planetary Science Letters*. 327-328, 1-8, doi:
950 10.1016/j.epsl.2012.01.007.

951

952 Wells, D.L., Coppersmith, K.J., 1994. New Empirical Relationships among Magnitude,
953 Rupture Length, Rupture Width, Rupture Area, and Surface Displacement. *Bulletin of the*
954 *Seismological Society of America*, **84**, 974–1002.

955

956 Yamaji, A., 2000. The multiple inverse method: a new technique to separate stresses from
957 heterogeneous fault-slip data. *Journal of Structural Geology*, **22**, 441–452.

958

959 Yardley, B.W.D. 1997. The evolution of fluids through the metamorphic cycle. In: Jamtveit,
960 B. & Yardley, B.W.D. (eds) *Fluid Flow and Transport in Rocks*. Chapman & Hall, 99-117.

961

962 Zoback M.D. Reservoir Mechanics (2007) Cambridge University Press, pp.449.

963

964

Table Caption

965 **Table 1:** XRD analyses from zeolite mineralized veins in the Lobbia Glacier Valley area. For

966 further details see Appendix 1.

967

Figure Captions

968 **Figure 1.** (a) Schematic geological map of the Adamello region. GLFZ = Gole Larghe Fault
969 Zone; PCFZ = Passo Cercen Fault Zone; LF = Lares Fault. Red box shows location of study
970 area. (b) Aerial photograph of the study area with numbered faults (NNE-SSW sinistral =
971 green (S); E-W sinistral-reverse = red (T); N-S normal = blue (N)). Black dashed contact and
972 yellow shaded zone are, respectively, the southern margin of the GLFZ and central zone of
973 K-feldspar-epidote-chlorite alteration according to Smith et al. (2013). Box shows location of
974 Figure 4. (c) An oblique aerial view looking S showing the typical appearance of the
975 fractured tonalities in the glacier valley. The largest fault, S1, lies in the centre of the valley.

976 **Figure 2.** Examples of fractures and zeolite mineralization. (a) Altered damage zone and vein
977 fracture meshes along fault N1. Oblique cross-section view. (b) Plan view of composite
978 tensile vein related to fault N3 with multi-coloured zeolite fills. Arrows show offset
979 trajectories (c) From E to W, wall rock, altered damage zone and core with red gouge in
980 cross-section view of sinistral fault S2. Note steep mylonitic foliation in both wall rock and
981 damage zone indicative of reactivation of a pre-existing sinistral shear zone.(d) Cross-
982 sectional view of linked fractures and altered damage zone along sinistral-reverse thrust fault
983 T1. Note linking sub-horizontal R-shears. Box shows location of Fig 3d. (e) Down-slope
984 view of prominent gulley feature following sinistral fault S3. Valley sides are defined by two
985 NNE-SSW sinistral faults (green) while the central region and wall rocks are cut by en-
986 echelon sets of N-S normal faults (blue). (f) Oblique section view of interlinked and cross-
987 cutting fracture sets (labelled) developed in the upper part of the GLFZ. Note the <2m
988 sinistral offset of fault T1 by S1 and the linkage of faults T1 and N3. The gouge injections
989 shown in Fig 6a occur at the latter junction.

990 **Figure 3.** Fracture kinematics, linkage and zeolite mineralization. (a) Shallowly-plunging
991 slickenlines (arrows) within zeolite-bearing gouge on a NNE-SSW sinistral fault related to
992 fault S3. Note earlier pale zeolite tensile fracture fill at the margins of the fault. (b) Plan-view
993 of zeolite-bearing composite fault zone related to fault S1 with breccia and gouge showing
994 prominent development of T-fractures consistent with sinistral shear. Note alteration halo in
995 wall rocks adjacent to fault. (c) View of steeply plunging slickenlines along zeolite vein
996 filling N-S normal fault associated with fault N3. (d) Close-up section view of SSW-dipping
997 slip surface in fault T1 with cm-scale, top-to-the-left offsets of the pale aplite vein along sub-
998 horizontal linking R-fractures in the fault hangingwall. Also shows orange-brown zeolite
999 gouges developed along the underlying slip surface and the pre-existing protomylonitic
1000 foliation reactivated by the E-W fault zone. (e) Plan view of linked NNE-SSW sinistral faults
1001 and N-S normal/tensile fractures (arrows). (f) Oblique view of slip surface showing

1002 overprinting dip-slip and later (sinistral) strike-slip slickenlines. Note that the fracture surface
1003 changes strike from N-S (right) to NNE-SSW (left) possibly marking the linkage of a N-S
1004 normal and NNE-SSW sinistral segment.

1005 **Figure 4.** Detailed map of the zeolite-bearing fracture patterns around fault S1 (see Fig. 1b).
1006 The density of fractures moving away from the main fault decreases, as do the fault damage
1007 zone thicknesses along the linking E-W sinistral reverse faults.

1008 **Figure 5.** Evidence for multiple slip-mineralization events. (a) Plan view of sheared and
1009 cataclastically deformed composite zeolite vein associated with fault N3. (b) Mineralized
1010 zeolite gouge with angular fragments of wall rocks and earlier pale zeolite veins. Plan view of
1011 fault N2.

1012 **Figure 6.** Zeolite-mineralized gouge injections. (a) Section view of gouge-filled N-S tensile
1013 fractures (arrowed) developed in footwall of the sinistral-reverse fault T1. Note that the T1
1014 slip surface is filled with the same gouge. (b) Sectional view of N-S tensile fractures filled
1015 with a least 2 phases of injected zeolite gouge (early pale coarser phase and later dark, finer
1016 phase). Located in the footwall of fault T3. (c) Sectional view of orange-red zeolite gouge-
1017 breccia with earlier zeolite, epidote cataclasite and granite clasts close to fault T3. (d) Section
1018 cut through a sample of the E-W zeolite T1 fault gouge shown in (a) highlighting multiple
1019 generations of gouge and injection events. The section is cut parallel to transport and the
1020 obliquity of the injections is consistent with the inferred sinistral-reverse shear sense.

1021 **Figure 7.** Microstructural development of zeolite mineralisation. All images are in cross-
1022 polars. (a) Zoned zeolite vein showing anhedral crystals towards the vein wall, acicular
1023 needles, and fine-grained acicular needles towards the centre of the vein. (b) Later shearing
1024 leading to cataclasis and the formation of suspended clasts of vein material. (c) Homogeneous
1025 zeolite cataclasite. (d) Crystalline haloed clasts of zeolite cataclasite suspended in a fine-
1026 grained zeolite gouge. (e) Tensile fracturing of a gouge (with haloed zeolite cataclasite clasts)
1027 forming a new zeolite vein at the right-hand margin. (f) Injection of fine grained zeolite
1028 gouge (highlighted by dashed lines) through a zeolite vein & cataclasite. (g) Repeated crack
1029 seal textures in a zeolite vein.

1030 **Figure 8.** Equal area stereoplots of pre-existing structures (cooling joints, aplite sheets, shear
1031 zone mylonites and cataclasites-pseudotachylytes) compared to the stereoplots showing the
1032 various zeolite-bearing fractures. The close similarities in orientation are consistent with the
1033 reactivation of the variously oriented pre-existing structures observed in the field. The
1034 structures are ordered in terms of their relative age and depth of formation, with those on the
1035 left forming first and at greatest depths (see Pennacchioni et al., 2006).

1036 **Figure 9.** Left and centre: kinematic data and paleostress inversion results for all zeolite-
1037 bearing brittle faults in the Lobbia Glacier valley. Right: Mohr plot representing the reduced
1038 (adimensional) deviatoric stress tensor (axes are in percent of σ_1); See Delvaux and Sperner
1039 (2003) for details. The calculated stress states for the NNE-SSW sinistral, N-S normal (both
1040 black) and E-W sinistral-reverse (red) faults are also shown.

1041 **Figure 10.** Stereographic (left) and Mohr plots (right) of Normalized Slip Tendency (NST;
1042 top) and Dilation Tendency (DT; bottom). Red = high NST or DT; blue = low NST or DT;

1043 pale blue dots = Andersonian orientations; white polygons = principal stress axes; white dots
1044 = poles to main fault sets.

1045 **Figure 11.** (a) Coulomb stress model M3 rupture events along NNE-SSW sinistral fault S1
1046 showing stress loading magnitudes (red = increase in Coulomb stress; blue = decrease in
1047 Coulomb stress) and local transient reorientations of horizontal displacement directions
1048 (arrows). (b) Basic fault map highlighting regions which have become more likely to fail
1049 because of the stress transfer associated with the rupture of S1. (c) Stereographic projection
1050 showing the rake of lineation (red dot) on the E-W sinistral-reverse faults predicted by the
1051 modelling in (a), compared to the lineations observed in the field (black dots). (d) 3D block
1052 diagram looking south showing the geometric relationships between the reactivation of pre-
1053 existing structures following stress transfer onto E-W faults.

1054 **Figure 12.** Graph showing the characteristic timescales (τ) for diffusion across a range of
1055 distances (500 to 10000 m). Hydraulic diffusivities (κ) are taken directly from: (a) estimates
1056 of the *in situ* macroscopic fluid diffusion tensor beneath the Afar rift (Noir *et al.*, 1997); and
1057 (e) *in situ* studies of fluid injection into geothermal reservoirs (Shapiro *et al.*, 2003), or
1058 derived from permeability values obtained from (b) modelling the aftershock propagation
1059 velocity following the Umbria-Marche earthquakes ($M_w = 5.7, 6$) (Miller *et al.*, 2004); (c and
1060 d) static measurements on small, zeolite- and calcite-bearing faults under a range of confining
1061 pressures (Walker *et al.*, 2013a, b); and (f) estimates for intraplate continental crust
1062 (Townend and Zoback, 2000). (b), (c), (d) and (f) assume porosity (ϕ) = 0.02, fluid
1063 compressibility (β_f) = $5 \times 10^{-10} \text{ Pa}^{-1}$, rock compressibility (β_r) = $2 \times 10^{-11} \text{ Pa}^{-1}$, and fluid
1064 viscosity (η) = $1.9 \times 10^{-4} \text{ Pas}$ (Townend and Zoback, 2000).

1065 **Figure 13.** Cartoon showing the proposed rupture-reativation-cementation cycle. Initially (i)
1066 deep seated tectonically-induced rupture allows (ii) fluids to enter the system. At this stage
1067 pre-existing structures are stable, but increasing stress and/or pore fluid pressure associated
1068 with rupturing along fault S1 eventually leads to other NNE-SSW and N-S orientated pre-
1069 existing structures being reactivated. Mineralisation of the fractures occurs (iii) as fluid
1070 pressures fall, leading to cementation and sealing. This reduces permeability allowing the re-
1071 establishment of high pore fluid pressures, restarting the rupture-reativation-cementation
1072 cycle (iv-vi, vii-ix, etc). The mainshocks (bigger) and aftershock (smaller) focal mechanisms
1073 shown are purely schematic with kinematics based on outcrop patterns and stress inversions.

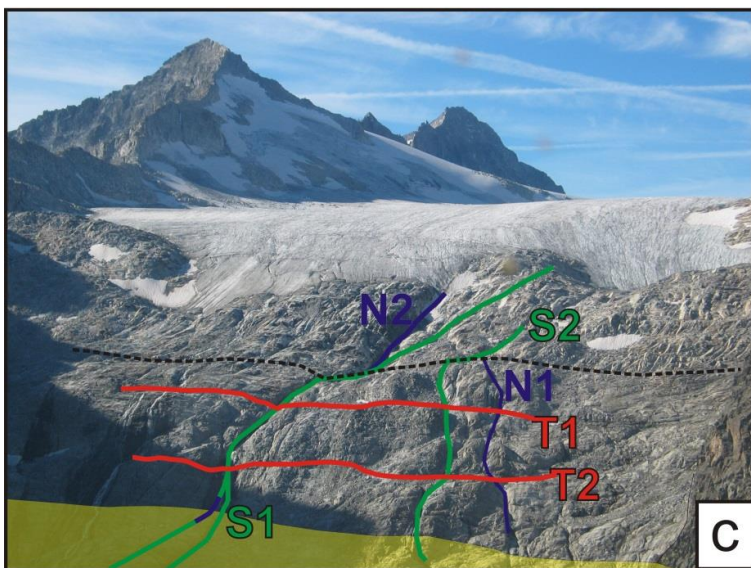
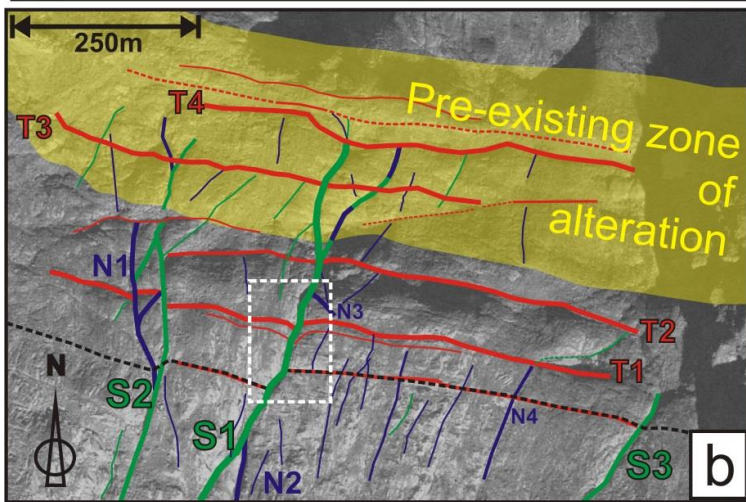
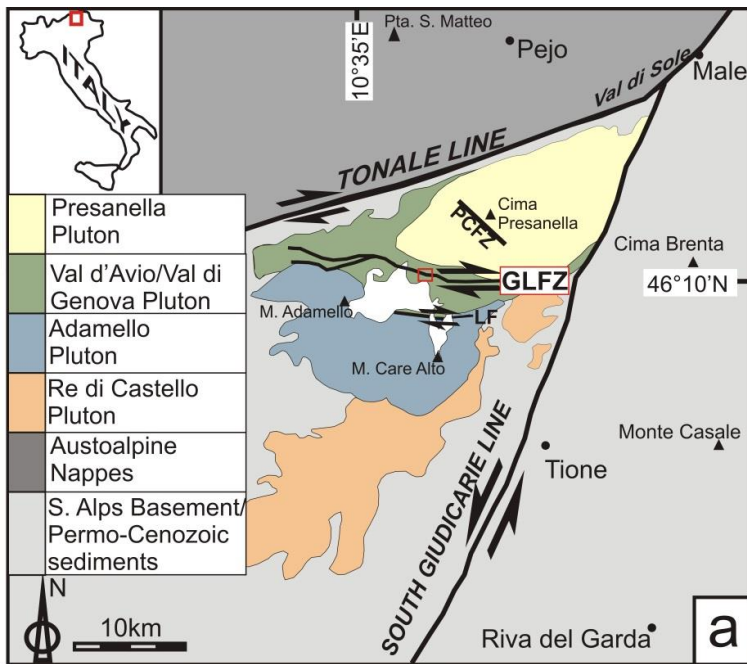


Fig 1

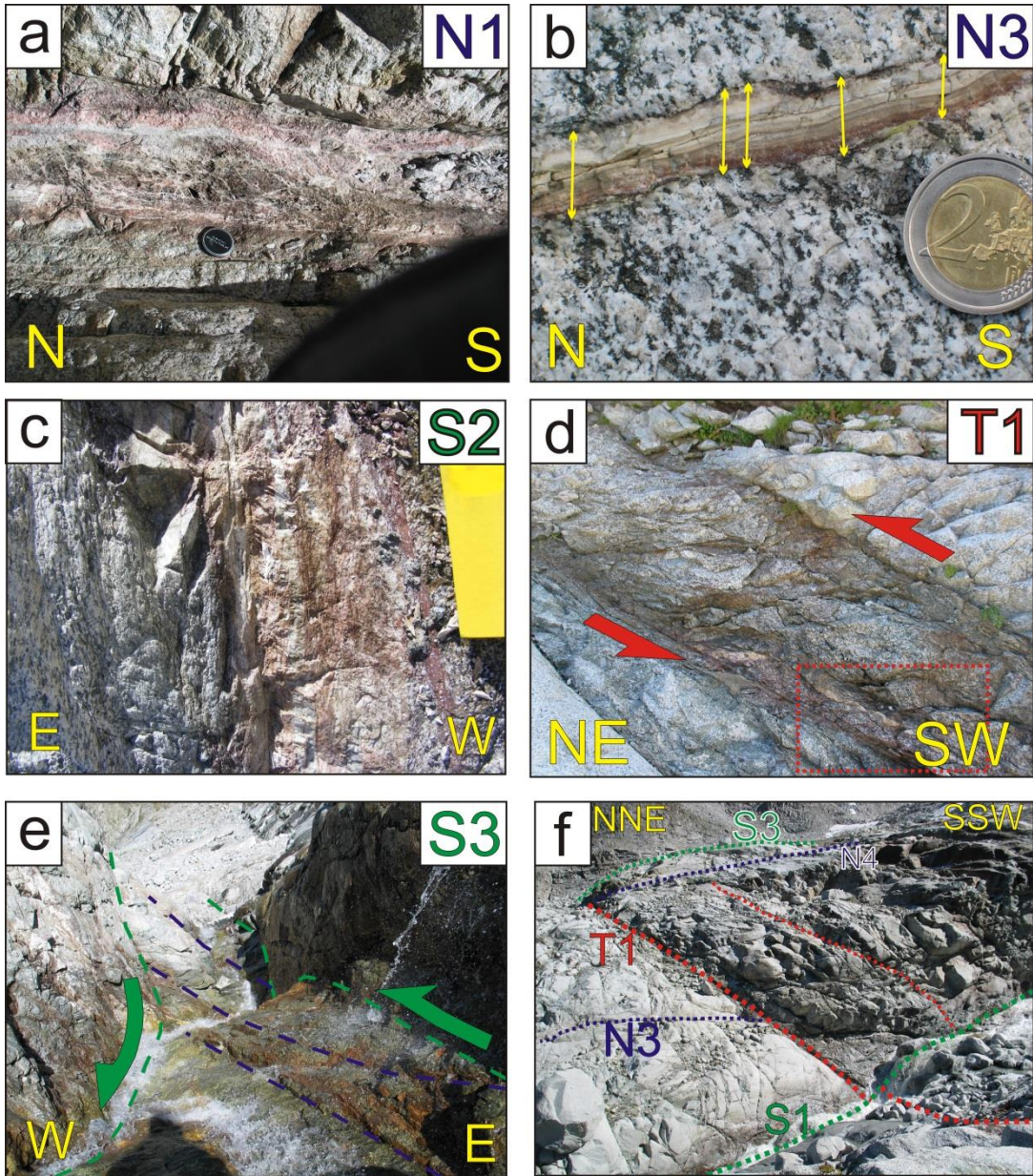


Fig 2

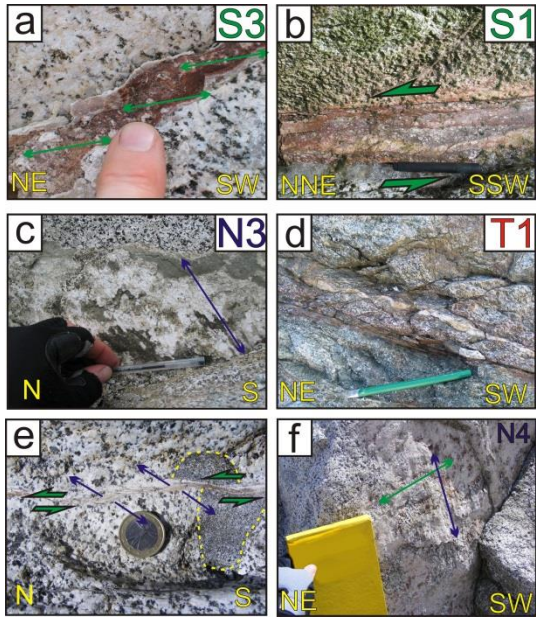


Fig 3

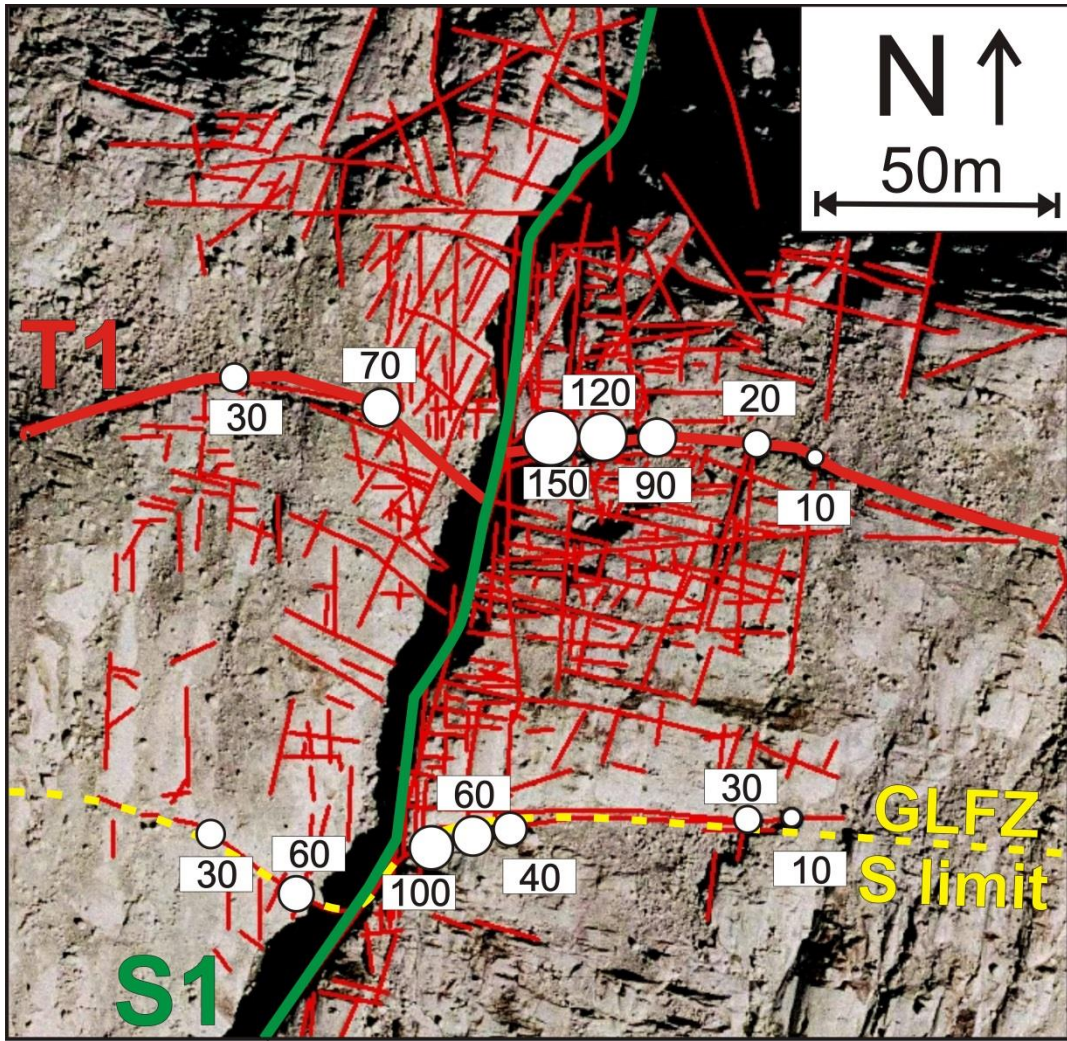


Fig 4



Fig 5

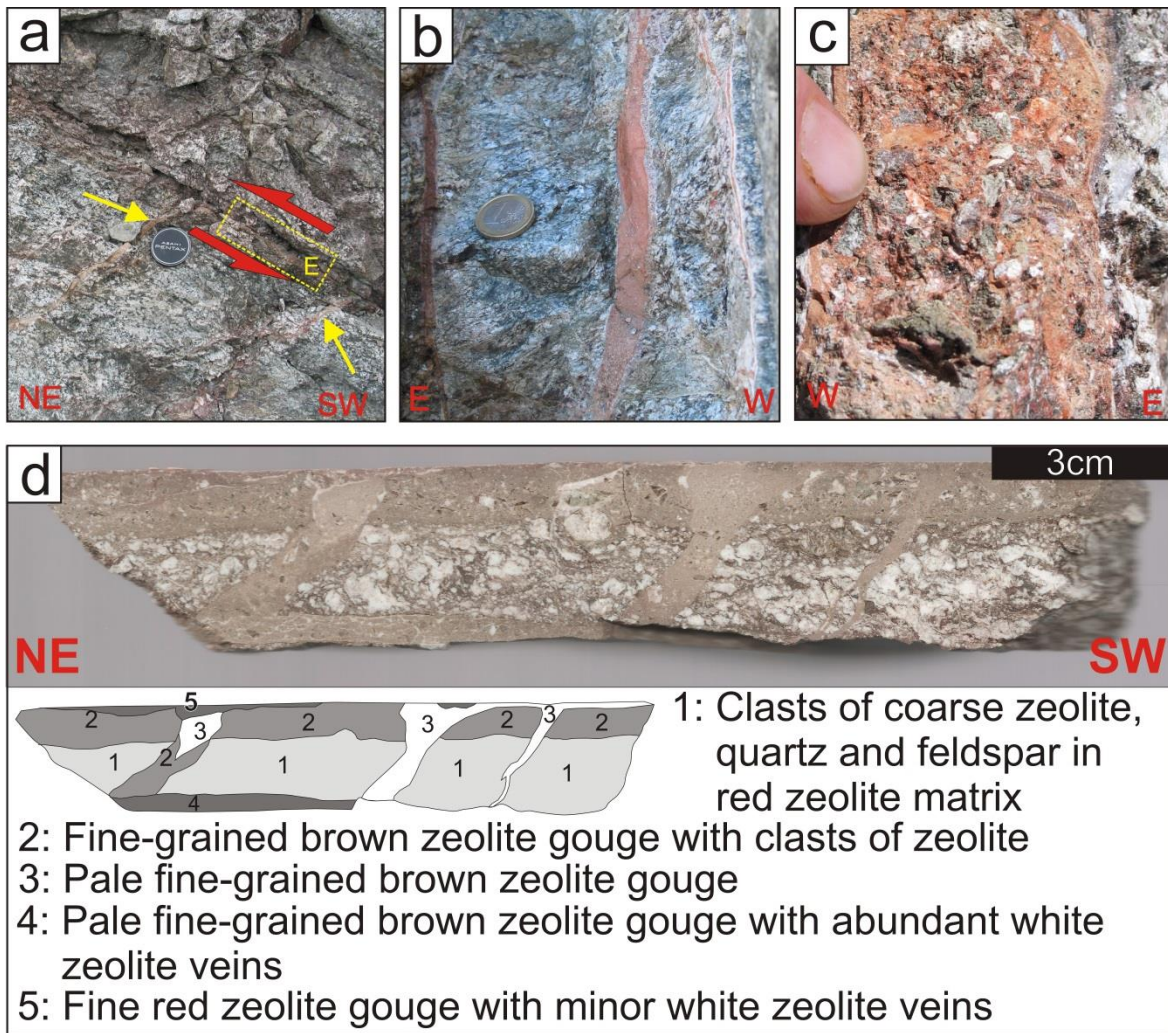


Fig 6

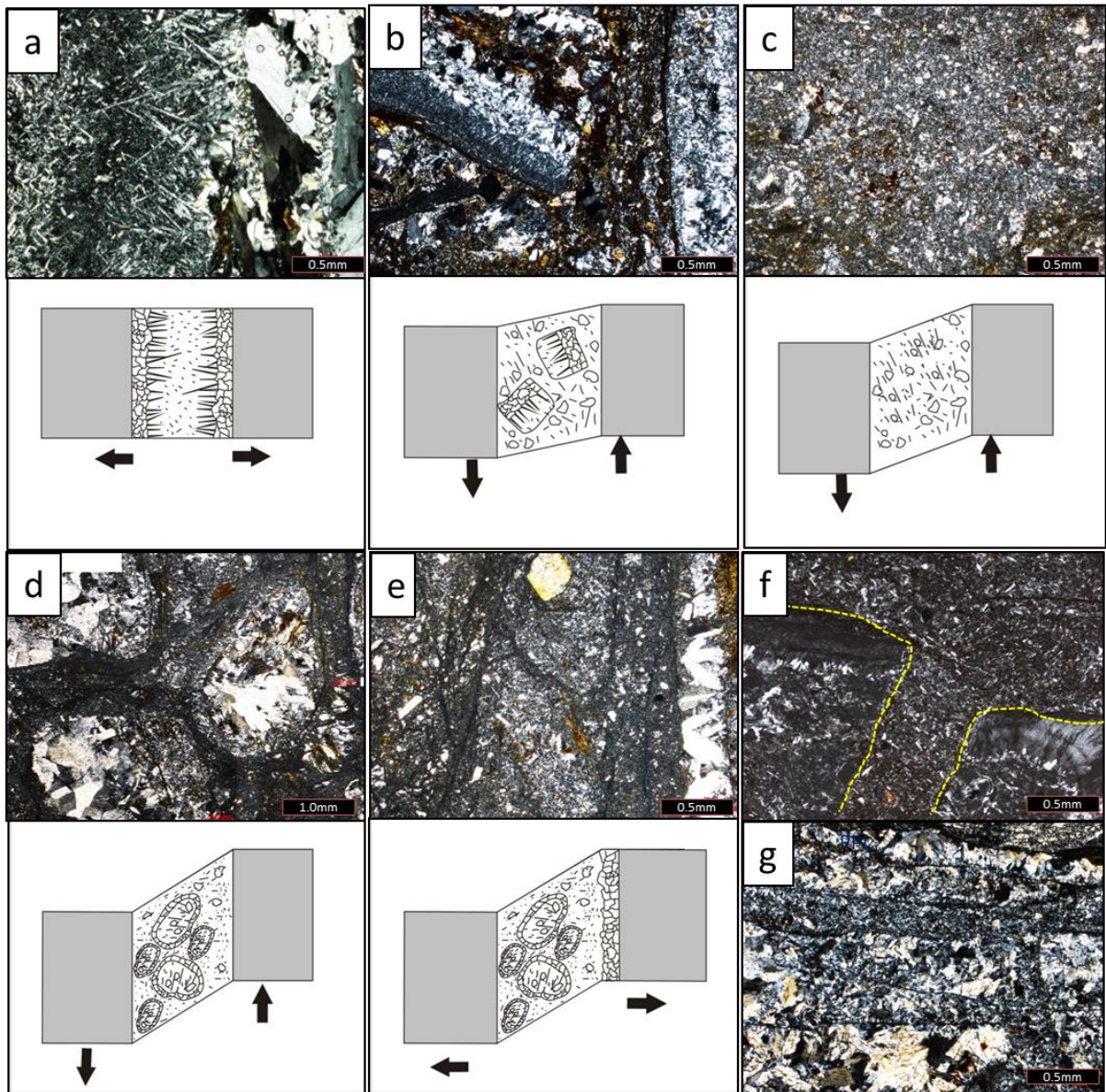


Fig 7

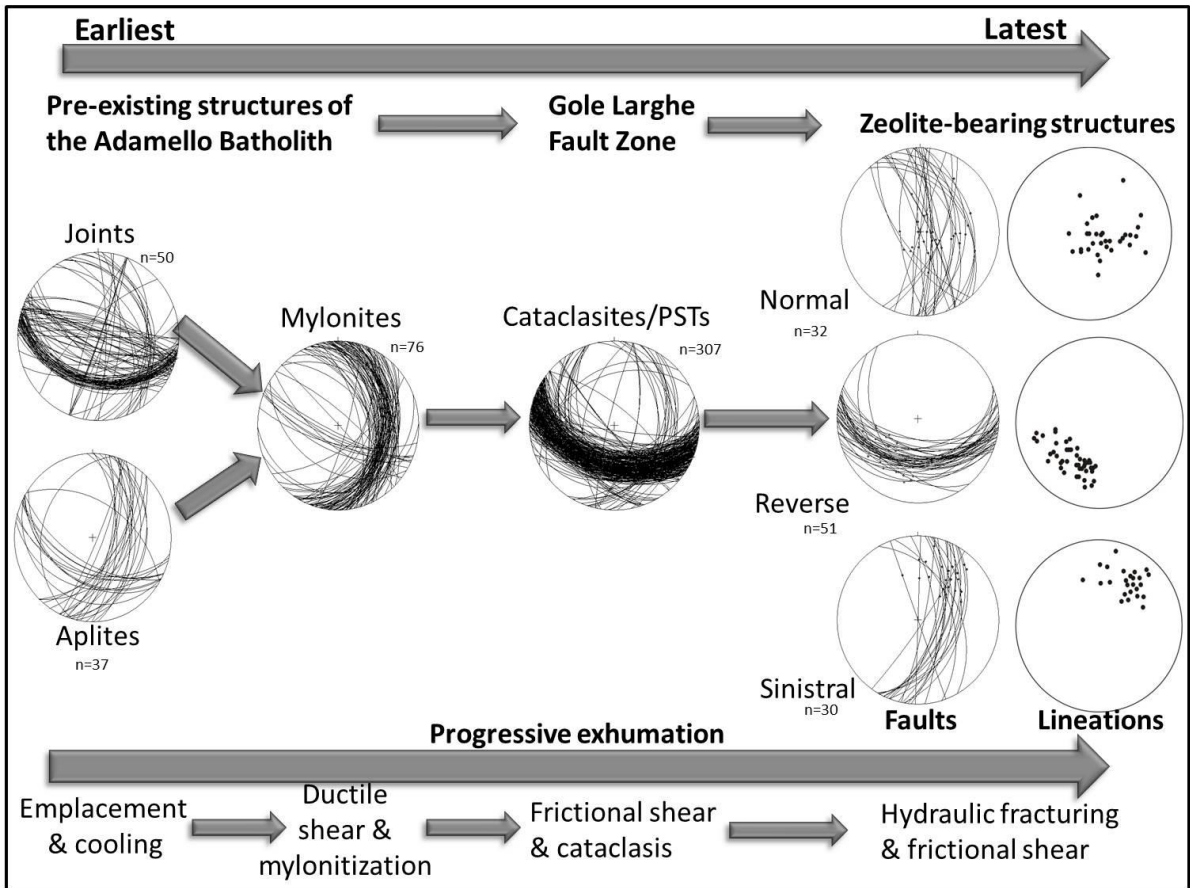


Fig 8

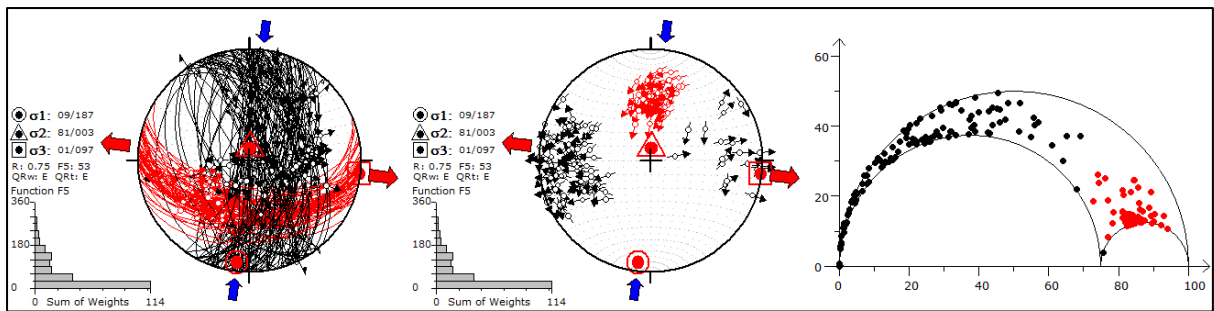


Fig 9

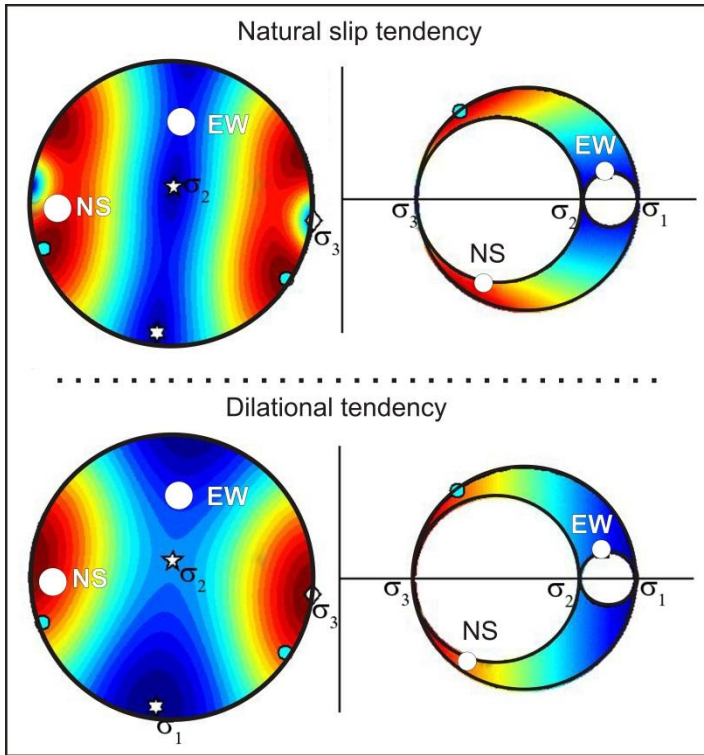


Fig 10

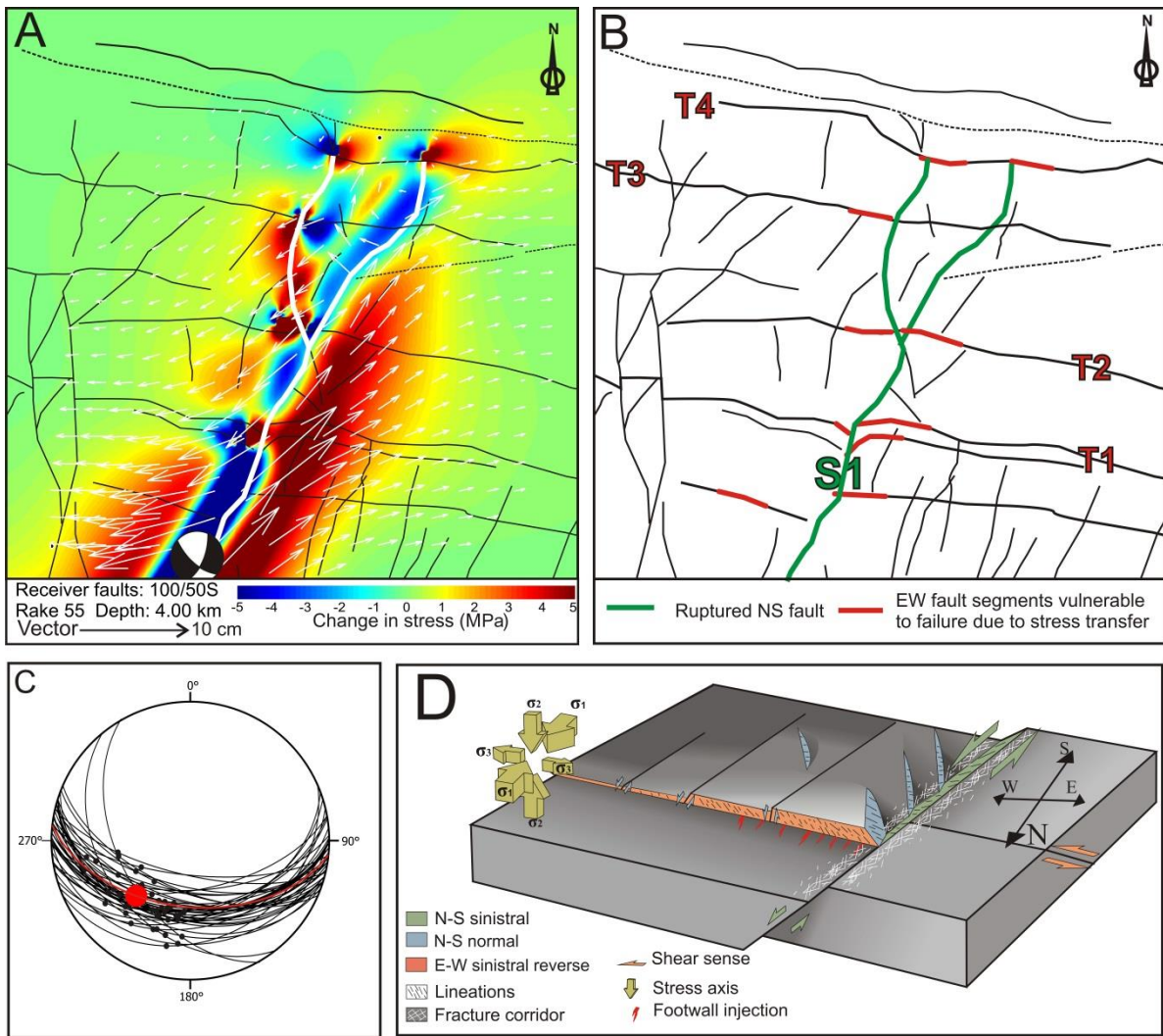


Fig 11

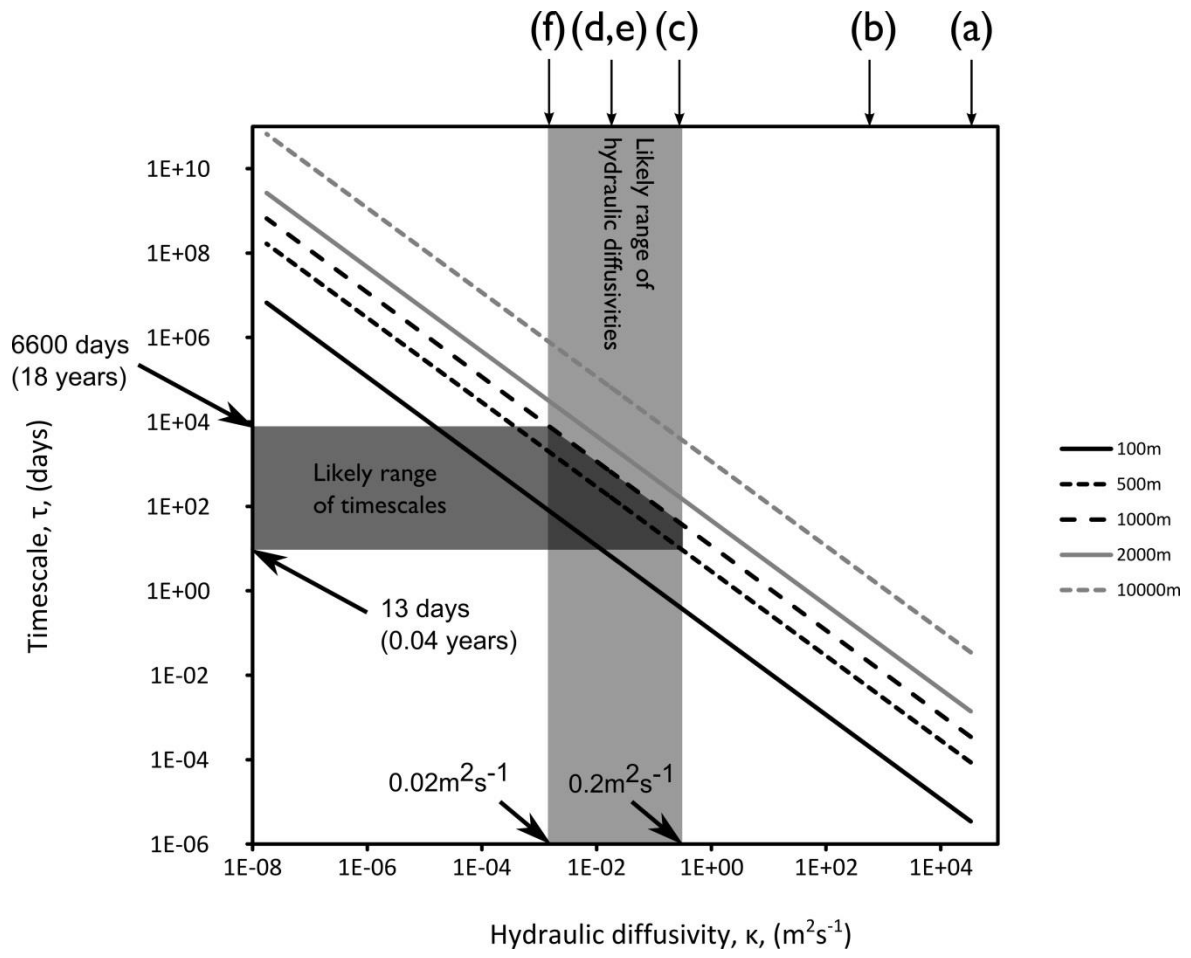


Fig 12

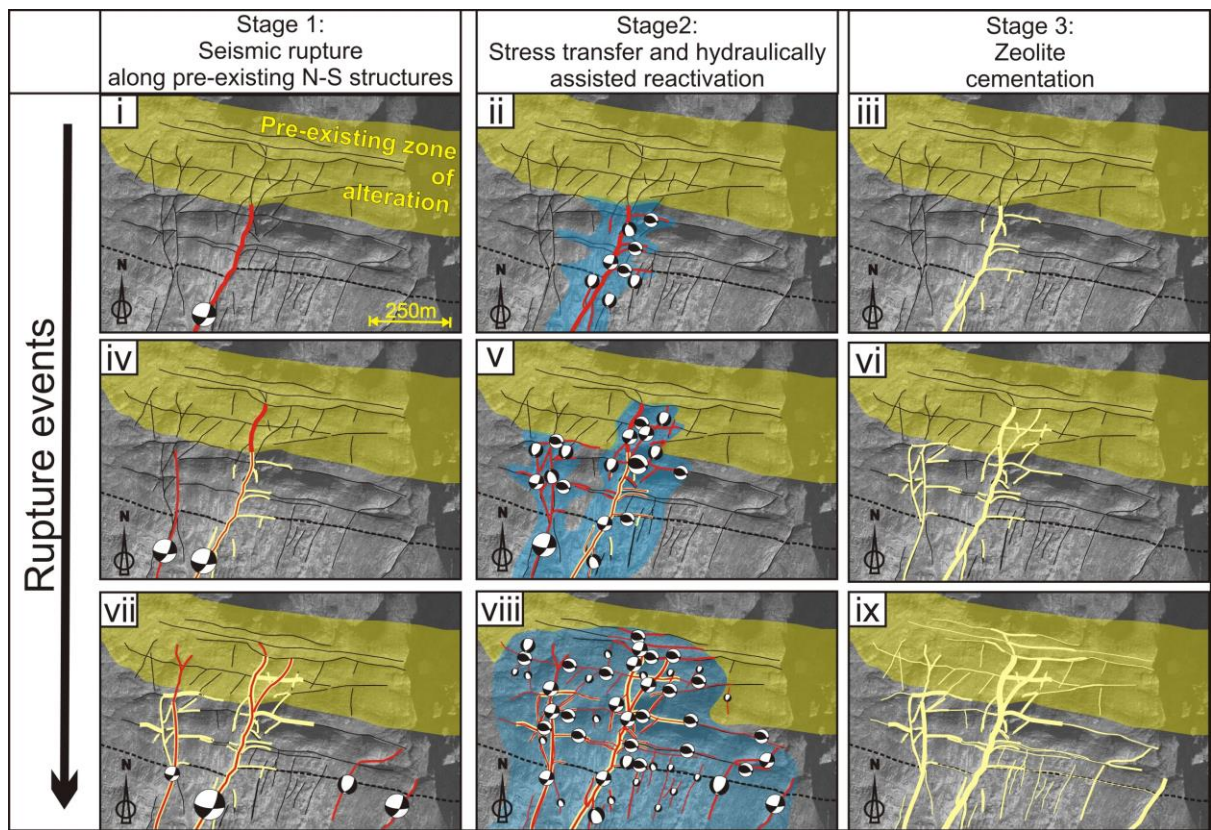


Fig 13

Fault type	E-W rev	E-W rev	E-W rev	E-W rev	E-W rev	E-W rev	N-S nml	N-S nml	N-S Sin	N-S Sin	N-S Sin	N-S Sin	N-S Sin	N-S Sin	E-W rev	
Fault	T1	T1	T1	T1	T1	T1	S1	S1	S1	S1	S1	S1	S1	S1	S2	T3
							fracture zone	fracture zone	fracture zone							
Sample	LFZ-1b	LFZ-1c1a	LFZ-1c1	LFZ-1c2	A03-07	A03-01	A03-04	A03-06	A03-05	LZF-20a	LZF-20b	LZF-20c	LZF20-d	LZF-13	LFZ-17b	

% Laumontite	72	62	30	62	57	45	0	34	20	88	50	40	48	36	87
% Stiblite	0	0	0	0	0	55	58	44	55	0	0	0	0	0	0
% Stellerite	0	38	0	0	0	0	0	0	0	0	0	0	0	0	0
% Scolecite	0	0	0	0	0	0	42	22	16	0	0	0	0	0	0
% Prehnite	15	0	15	17	7	0	0	0	0	0	0	0	0	0	0
% Chlorite	8	0	9	13	7	5	0	0	0	0	0	0	0	7	3
% Quartz	5	0	10	8	29	0	0	0	9	0	0	0	6	27	10
% Albite	0	0	36	0	0	0	0	0	0	0	0	0	0	0	0
% K-Feldspar	0	0	0	0	0	0	0	0	0	12	50	60	46	31	0

Table 1

1 **APPENDIX 1**

2 *Mineralogical analyses*

3 X-Ray diffraction analysis (XRD) was performed at the Dipartimento di Geoscienze (Padua
4 University) on powdered samples of the fault zone rocks (vein fills, gouges, cataclasites and
5 ultracataclasites initially distinguished based on their colour in the field, e.g. Fig. 2b-c, 3e, 5a,
6 6c, 6d). All the samples were ground to a particle size $<10\ \mu\text{m}$ to minimize possible micro-
7 absorption effects and to improve accuracy in measuring the intensities. X-ray powder
8 diffraction data were recorded on a Panalytical θ - θ diffractometer (Cu radiation) equipped
9 with a long fine focus Cu X-ray tube (operating at 40kV and 40mA), sample spinner, Ni filter
10 and a solid state detector (X'Celerator). The system optics consist of fixed $\frac{1}{2}^\circ$ divergent slit
11 and 1° antiscatter slit on the incident beam path and soller slits (0.04 rad) on incident and
12 diffracted beam path. The powders were mounted on 32 mm (internal diameter) circular
13 sample holder. Scans were performed over the range 3 - $80^\circ\ 2\theta$ with a virtual step size of
14 $0.017^\circ\ 2\theta$ and a counting time of 100 s/step. The phase identification and semi-quantitative
15 analysis were performed using the software package X'Pert HighScore Plus. The phase
16 identification was gained by the comparison with the reference pattern database Panalytical-
17 ICSD (Inorganic Crystal Structure Database). The semi-quantitative data were calculated
18 through the normalized RIR (Reference Intensity Ratio) method (Chung, 1974), using the
19 scale factor measured and RIR values from ICSD database.

20 The XRD mineral abundances are reported in Table 1, but remain indicative and not
21 necessary representative of the entire fault/fracture system. The error in weight % may range
22 between $\pm 1\%$ to $\pm 5\%$ depending on the number and type of minerals in the powder (e.g.,
23 phyllosilicates and clay minerals might be overestimated given their preferred orientation
24 under the X-ray beam). The large scatter in the mineral abundance of individual samples

25 might also be due to the sampling technique: a representative analysis of the vein filling
26 would have required a systematic sampling of each fault/fracture set, but this was not the goal
27 of our study. The main minerals found (Table 1) were zeolites (the Ca-rich stilbite, scolecite
28 and stellerite plus the Na- and Ca-rich laumontite), and prehnite plus quartz, albite, chlorite
29 and K-feldspar (the latter four inside clasts of tonalite and sub-greenschist facies cataclasites:
30 see for example Fig. 3a). The RIR semi-quantitative analysis showed variations in zeolite
31 mineralogy and abundance depending on the type of fault (T, S and N, Fig. 1), fracture type
32 (pure tensile or sheared) and host rock. For instance, if the occurrence of laumontite was
33 widespread and independent of fault orientation (with the exception of sample A3-04 from
34 S1), stilbite and scolecite were found only in the fillings of tensional fractures of the strike-
35 slip (S) and normal faults (N). Conversely, samples taken from the thrust (T) group always
36 included quartz (e.g., A03-07), whilst injection veins departing from the same T faults carry
37 little or no quartz (sample A03-01). Multiple zeolite mineralization events (sample LFZ-1 in
38 Fig. 6d) had almost the same zeolite mineralogy. The mineralogy of the zeolite-bearing veins
39 also reflected the composition of the host-rocks. For instance, the zeolite-bearing faults
40 exploiting aplite vein contacts were enriched in albite (sample LFZ-13 from fault T3) or those
41 exploiting the sub- greenschist facies cataclasites were enriched in chlorite and quartz
42 (sample A03-07 from T1).